Geophys. J. Int. (2006) **167,** 705–736 doi: 10.1111/j.1365-246X.2006.03095.x

Body-wave traveltime and amplitude shifts from asymptotic travelling wave coupling

F. Pollitz

US Geological Survey, Menlo Park, CA 94025, *USA. E-mail: fpollitz@usgs.gov*

Accepted 2006 May 18. Received 2006 April 26; in original form 2005 December 28

SUMMARY

We explore the sensitivity of finite-frequency body-wave traveltimes and amplitudes to perturbations in 3-D seismic velocity structure relative to a spherically symmetric model. Using the approach of coupled travelling wave theory, we consider the effect of a structural perturbation on an isolated portion of the seismogram. By convolving the spectrum of the differential seismogram with the spectrum of a narrow window taper, and using a Taylor's series expansion for wavenumber as a function of frequency on a mode dispersion branch, we derive semi-analytic expressions for the sensitivity kernels. Far-field effects of wave interactions with the free surface or internal discontinuities are implicitly included, as are wave conversions upon scattering. The kernels may be computed rapidly for the purpose of structural inversions. We give examples of traveltime sensitivity kernels for regional wave propagation at 1 Hz. For the direct *SV* wave in a simple crustal velocity model, they are generally complicated because of interfering waves generated by interactions with the free surface and the Mohorovičić discontinuity. A large part of the interference effects may be eliminated by restricting the travelling wave basis set to those waves within a certain range of horizontal phase velocity.

Key words: body waves, Born approximation, scattering, travelling waves, traveltime, wave propagation.

1 INTRODUCTION

Classical body-wave tomography is based on a simple relationship between a traveltime T and velocity structure v (**r**):

$$T = \int_\Gamma \frac{1}{v(\mathbf{r})}\, ds, \tag{1}$$

where $v(\mathbf{r})$ is the wave speed of the propagating wave, the line integral is taken over the path Γ between source and receiver, and ds is the length element along the ray path. If $v(\mathbf{r})$ is a perturbation about a reference velocity structure $v_0(\mathbf{r})$, then eq. (1) may be recast as

$$\delta T = T - T_0 = -\int_\Gamma \frac{\delta v}{{v_0}^2(\mathbf{r})}\, ds, \tag{2}$$

$$T_0 = \int_\Gamma \frac{1}{v_0(\mathbf{r})}\, ds, \tag{3}$$

where $\delta v(\mathbf{r}) = v(\mathbf{r}) - v_0(\mathbf{r})$. Fermat's principle states that eq. (2) is valid to first order in δv when Γ is the ray path traversed on the unperturbed model.

Consideration of wave propagation through a laterally heterogeneous medium demonstrates that eq. (2) is valid only if the velocity structure is sufficiently smooth, that is, it varies only on a length scale that is large compared with the wavelength and the width of the Fresnel zone (e.g. Romanowicz 1987; Dahlen *et al.* 2000; Zhao *et al.* 2000). The relationship between δT and structural perturbations at finite wavelength (or equivalently, finite frequency) involves sensitivity to velocity structure over a volume surrounding Γ of a width of a few wavelengths (e.g. Yomogida & Aki 1987; Woodward 1992; Marquering *et al.* 1999; Hung *et al.* 2000; Zhao *et al.* 2000). This assumes that a particular seismic phase can be isolated within the time window of interest; the sensitivity can extend over a much wider region if several wave types and/or wave conversions are involved. For an aspherical model involving perturbations in shear modulus μ, bulk modulus κ and density ρ, the traveltime shift measured at a receiver **r** is a sum of integrals of structural perturbations weighted by corresponding sensitivity

kernels:

$$\delta T(\omega) = \int \left[K_{\mu}^{(\delta T)}(\omega; \mathbf{r}, \mathbf{r}')\delta\mu(\mathbf{r}') + K_{\kappa}^{(\delta T)}(\omega; \mathbf{r}, \mathbf{r}')\delta\kappa(\mathbf{r}') + K_{\rho}^{(\delta T)}(\omega; \mathbf{r}, \mathbf{r}')\delta\rho(\mathbf{r}')\right] d^3\mathbf{r}'. \quad (4)$$

An analogous expression for the amplitude shift is

$$\delta(\ln A)(\omega) = \int \left[K_{\mu}^{(\delta(\ln A))}(\omega; \mathbf{r}, \mathbf{r}')\delta\mu(\mathbf{r}') + K_{\kappa}^{(\delta(\ln A))}(\omega; \mathbf{r}, \mathbf{r}')\delta\kappa(\mathbf{r}') + K_{\rho}^{(\delta(\ln A))}(\omega; \mathbf{r}, \mathbf{r}')\delta\rho(\mathbf{r}')\right] d^3\mathbf{r}'. \quad (5)$$

If the aspherical model is parametrized in terms of velocity perturbations $\delta v(\mathbf{r}')$ then one may define sensitivity kernels with respect to velocity:

$$\delta T(\omega) = \int K_{\delta v}^{(\delta T)}(\omega; \mathbf{r}, \mathbf{r}')\, \delta v(\mathbf{r}')\, d^3\mathbf{r}', \quad (6)$$

$$\delta(\ln A)(\omega) = \int K_{\delta v}^{(\delta(\ln A))}(\omega; \mathbf{r}, \mathbf{r}')\, \delta v(\mathbf{r}')\, d^3\mathbf{r}'. \quad (7)$$

Methods which express the relationship between finite-frequency traveltimes and amplitudes and 3-D velocity structure are based on normal mode coupling (e.g. Marquering *et al.* 1999; Zhao *et al.* 2000) and finite frequency ray theory (Dahlen *et al.* 2000; Zhao *et al.* 2000). The geometrical ray-theoretical treatments of Dahlen *et al.* (2000) and Section 3 of Zhao *et al.* (2000) especially allow rapid computation of the kernels of eq. (4), allowing the practical computation of such kernels for numerous source–receiver configurations and the interpretation of large traveltime data sets.

The purpose of this paper is to develop an efficient means of synthesizing sensitivity kernels with respect to a spherically symmetric reference model based on coupled travelling wave theory. Although this approach may afford no advantage over the ray-theoretical approach at large offsets where body wave phases are relatively easily isolated, it may be more convenient at the shorter offsets encountered in regional tomography where interfering phases are more likely to be present in the scattered wavefield. Zhao *et al.* (2000) (p. 568) note, 'However, when the reference model has internal discontinuities, especially those with significant impedance contrasts such as the Moho, $\cdots$, the rays that may have substantial contributions to the result become more numerous and it is a daunting task for ray theory to identify the rays of significance and then deal with them individually.' The present approach removes the need to identify incident and scattered rays (other than that of the target wave), as synthesized in ray-theoretical solutions, when considering which wave configurations produce scattered wave energy arriving within a specific time window. This advantage is shared by the normal mode approach taken in section 4 of Zhao *et al.* (2000), but the computational cost of straightforwardly evaluating all required normal mode coupling interactions is enormous.

Starting with coupled travelling wave theory (e.g. Snieder & Romanowicz 1988; Friederich 1999), and using a truncated Taylor's series expansion of wavelength as a function of frequency along a dispersion branch, we develop semi-analytic expressions for the first-order perturbation of complex amplitude of an isolated wave group in the frequency domain. This translates into amplitude and phase perturbations, hence a traveltime perturbation, of a wave group at finite frequency in a selected time window. Because of the use of travelling waves and the employed approximations for integrals of frequency involving pairs of dispersion branches, the resulting treatment is very efficient and suitable for structural inversions of large traveltime data sets.

2 PRELIMINARIES

We define the Fourier transform of a function $f(t)$ as

$$F(\omega) = \mathcal{F}[f(t)]|_{\omega} = \int_{-\infty}^{\infty} f(t)\, \exp[-i\omega t]\, dt. \quad (8)$$

The corresponding inverse Fourier transform is given by

$$f(t) = \mathcal{F}^{-1}[F(\omega)]|_{\omega} = \frac{1}{2\pi}\int_{-\infty}^{\infty} F(\omega)\, \exp[i\omega t]\, d\omega. \quad (9)$$

The convolution of two functions $F(\omega)$ and $G(\omega)$ is written as

$$F(\omega) * G(\omega) = \int_{-\infty}^{\infty} F(\omega')G(\omega - \omega')\, d\omega. \quad (10)$$

We shall make use of the Convolution Theorem:

$$\mathcal{F}\,[f(t)g(t)]|_{\omega} = \int_{-\infty}^{\infty} f(t)g(t)\, \exp[-i\omega t]\, dt = \frac{1}{2\pi}F(\omega) * G(\omega). \quad (11)$$

If one of the functions, say $g(t)$, is non-zero only in the finite interval $t_1 < t < t_2$, then eq. (11) reads

$$\int_{t_1}^{t_2} f(t)g(t)\, \exp[-i\omega t]\, dt = \frac{1}{2\pi}F(\omega) * G(\omega). \quad (12)$$

3 TRAVELLING WAVE REPRESENTATION OF SEISMIC SPECTRA

3.1 Displacement spectrum on laterally homogeneous model

A 1-D (i.e. spherically symmetric) reference model is specified on an isotropic, non-gravitating, non-rotating earth model by

$$\oplus = [\mu_0(r), \kappa_0(r), \rho_0(r), Q_\mu(r), Q_\kappa(r)], \tag{13}$$

as a function of radius. These are shear modulus, bulk modulus, density, and the shear and bulk Q, respectively. Working in a $\mathbf{r} = (r, \Delta, \phi)$ spherical coordinate system, the seismic displacement at angular frequency ω on this reference model is written as a sum of travelling waves (Dahlen & Tromp 1998; Pollitz 1998; Friederich 1999):

$$\begin{aligned}\mathbf{u}_0(\mathbf{r}, \omega) = &\sum_n [U_n(r)\hat{\mathbf{r}} + V_n\nabla_1]\,\psi_n^0(\hat{\mathbf{r}}, \omega) \\ &+ [-W_n(r)\hat{\mathbf{r}}\times\nabla_1]\,\psi_n^0(\hat{\mathbf{r}}, \omega),\end{aligned} \tag{14}$$

where $\hat{\mathbf{r}} = (\Delta, \phi)$ is the position vector on the unit sphere and

$$\nabla_1 = \frac{\partial}{\partial\Delta}\hat{\Delta} + (\sin\Delta)^{-1}\frac{\partial}{\partial\phi}\hat{\phi}, \tag{15}$$

is the surface gradient operator. The mode index n represents Rayleigh wave (spheroidal mode equivalent) and Love wave (toroidal mode equivalent) dispersion branches. The eigenfunctions $U_n(r)$ and $V_n(r)$ are zero for a Love wave, and $W_n(r)$ is zero for a Rayleigh wave. These functions are to be evaluated at the 'eigendegree' l_n on the dispersion branch of index n such that the analytically continued free oscillation dispersion relation yields ω for that dispersion branch, that is,

$$\omega_n(l_n) = \omega. \tag{16}$$

It is useful to define the wavenumber

$$\nu_n = l_n + \frac{1}{2}. \tag{17}$$

Because of the effect of attenuation, ν_n will lie just below the positive real axis in the complex wavenumber plane (e.g. Appendix A of Friederich 1999). ψ_n^0 is a potential function on the unit sphere which depends on the source parameters and the source–receiver geometry. We take the normalization convention of the eigenfunctions to be

$$\omega^2\int_0^R \left[U_n^2(r) + l_n(l_n+1)\left(V_n^2(r) + W_n^2(r)\right)\right] r^2\,dr \;=\; 1, \tag{18}$$

where R is the radius of the spherical elastic model. Assuming a point source located at $\mathbf{r}_0$ with spherical coordinates $(r = r_0, \Delta = 0)$ (Fig. 1), the response to a moment tensor source is (Pollitz 1998; Friederich 1999)

$$\begin{aligned}\psi_n^0(\hat{\mathbf{r}}, \omega) = -\frac{\pi i}{2}\frac{\nu_n c_n}{U_n}(\nu_n/2\pi)^{\frac{1}{2}}\left(\frac{\Delta}{\sin\Delta}\right)^{\frac{1}{2}} &\times \left[\Sigma_1 H_0^{(2)}(\nu_n\Delta)\right. \\ &\left.+ (\Sigma_2 - \Sigma_4)H_1^{(2)}(\nu_n\Delta) + (\Sigma_3 - \Sigma_5)H_2^{(2)}(\nu_n\Delta)\right],\end{aligned} \tag{19}$$

where $c_n = \omega/\nu_n$ is phase velocity, U_n is group velocity, the Σ-functions $\Sigma_j(r_0, \phi\,;\mathbf{M})$ are given by eq. (13) of Dahlen (1980) for excitation by a point source with moment tensor $\mathbf{M}$ (ω), and $H_m^{(2)}$ is the Hankel function of the second kind of order m. For an impulsive source, $\mathbf{M}(t) = \mathbf{M}H(t)$, and $\mathbf{M}(\omega) = \mathbf{M}/(i\,\omega)$. The excitation functions Σ_j are non-zero for Rayleigh waves for $j = 1, 2, 3$ and non-zero for Love waves for $j = 4, 5$. Eq. (19) accounts for the first orbit of the travelling wave decomposition (i.e. equivalent first-arriving surface waves) and is uniformly valid in the interval $0 < \Delta < \pi - \epsilon$, for $\nu_n\epsilon \gg 1$.

3.2 Displacement spectrum on laterally heterogeneous model

To describe wave propagation on the laterally heterogeneous earth, we identify a volume V as containing variations of structural parameters from the reference model $\oplus$. We parametrize 3-D perturbations in shear modulus, bulk modulus and density as

$$\delta\oplus = \{\delta\mu(\mathbf{r}), \delta\kappa(\mathbf{r}), \delta\rho(\mathbf{r})\} \quad \mathbf{r}\in V. \tag{20}$$

We consider that $\delta\oplus$ is inclusive of perturbations in both the bulk properties of the medium as well the locations of internal discontinuities.

We again place a point source at $\mathbf{r}_0$ with spherical coordinates $(r = r_0, \Delta = 0)$, and let $\mathbf{r}$ denote the position of a receiver on the sphere. From completeness of the basis set used to describe wave propagation on $\oplus$, the displacement spectrum at $\mathbf{r}$ on the model $\oplus + \delta\oplus$ may be written in the form

$$\begin{aligned}\mathbf{u}(\mathbf{r}, \omega) = &\sum_n [U_n(r)\hat{\mathbf{r}} + V_n\nabla_1]\,\psi_n(\hat{\mathbf{r}}, \omega) \\ &+ [-W_n(r)\hat{\mathbf{r}}\times\nabla_1]\,\psi_n(\hat{\mathbf{r}}, \omega).\end{aligned} \tag{21}$$

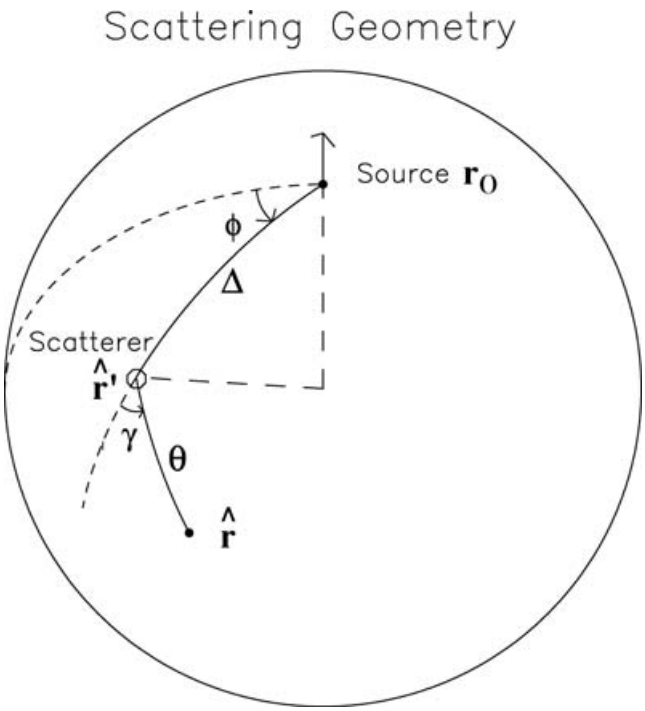

Figure 1. Scattering geometry for scatterer $\hat{\mathbf{r}}'$ to receiver $\hat{\mathbf{r}}$ interactions, with angular distance θ and azimuth γ. From source $\mathbf{r}_0$ to scatterer $\hat{\mathbf{r}}'$, the angular distance and azimuth are Δ and ϕ, respectively.

The aspherical potentials ψ_n obey an integral equation (e.g. Friederich 1999)

$$\psi_n(\hat{\mathbf{r}},\omega) = \psi_n^0(\hat{\mathbf{r}},\omega) + \frac{i}{4c_nU_n}\sum_{n'}\int\left(\frac{\theta}{\sin\theta}\right)^{\frac{1}{2}} \times\sum_{m=0}^{2}(-\nu_n)^m H_m^{(2)}(\nu_n\theta)\left[\delta\omega_{nn'}^{(m)}(\hat{\mathbf{r}}')(\sqrt{2}H_+)^m\right]\psi_{n'}(\hat{\mathbf{r}}',\omega)\,d^2\hat{\mathbf{r}}', \tag{22}$$

where

$$\sqrt{2}H_+ = \exp(i\gamma)\left(-i\cot\Delta\frac{\partial}{\partial\gamma} - \frac{\partial}{\partial\Delta} + \frac{i}{\sin\Delta}\frac{\partial}{\partial\phi}\right). \tag{23}$$

In eqs (22) and (23), referring to Fig. 1, Δ and ϕ are the colatitude and longitude of a scatterer at $\hat{\mathbf{r}}'$ on the unit sphere as measured from the source epicentre with $\cos\Delta = \hat{\mathbf{r}}'\cdot(\mathbf{r}_0/r_0)$; θ and γ are the scatterer–receiver distance and azimuth with $\cos\theta = \hat{\mathbf{r}}'\cdot\hat{\mathbf{r}}$ and γ measured positive counter-clockwise from due South, the southward extension of the source-scatterer great circle corresponding to $\gamma = 0$. The interaction kernels $\delta\omega_{nn'}^{(m)}(\hat{\mathbf{r}}')$ depend linearly on the structural perturbations $\delta\mu$, $\delta\kappa$, and $\delta\rho$ and are specified in Appendix A of Friederich (1999). The integration in eq. (22) is to be taken over that portion of the unit sphere that encompasses all perturbations in structural parameters.

3.3 Born approximation

Eq. (22) represents a system of coupled integral equations in the set of aspherical wavefield potentials $\{\psi_n\}$. The solution for these potentials is generally non-linear with respect to $\delta\mu$, $\delta\kappa$ and $\delta\rho$. To determine Fréchet derivatives it is useful to evaluate the solution for the $\{\psi_n\}$ to first order in the structural perturbations. This is accomplished by substituting the laterally homogeneous wavefield potentials $\psi_{n'}^0$ into the right-hand side of eq. (22).

$$\psi_n(\hat{\mathbf{r}},\omega) = \psi_n^0(\hat{\mathbf{r}},\omega) + \frac{i}{4c_nU_n}\sum_{n'}\int\left(\frac{\theta}{\sin\theta}\right)^{\frac{1}{2}} \times\sum_{m=0}^{2}(-\nu_n)^m H_m^{(2)}(\nu_n\theta)\left[\delta\omega_{nn'}^{(m)}(\hat{\mathbf{r}}')(\sqrt{2}H_+)^m\right]\psi_{n'}^0(\hat{\mathbf{r}}',\omega)\,d^2\hat{\mathbf{r}}'. \tag{24}$$

Although eq. (24) is generally highly inaccurate for the determination of seismic waveforms at high frequency and/or large degrees of lateral heterogeneity, it is applicable to the determination of phase changes under certain conditions. For a very smooth lateral heterogeneity, it can be shown (e.g. Pollitz 1994) that multiple forward scattering evaluated using the stationary-phase approximation reduces to classical ray theory for the traveltime of any isolated seismic wave arrival. In addition, the associated phase change is the sum of the phase shifts that would be obtained by first-order scattering theory. More generally the validity of the Born approximation for traveltime has been investigated by

Baig *et al.* (2003) by considering wave propagation through a random medium. Zhao *et al.* (2000) note that the Born approximation is implicit in any treatment that involves calculating Fréchet kernels with respect to a reference model. The validity of the approach ultimately depends upon the adequacy of the reference model (Zhao *et al.* 2005). The present investigation is restricted to a spherically symmetric reference model.

4 ASYMPTOTIC EVALUATION OF TRAVELLING WAVE SIGNALS

The use of travelling waves to represent seismic wave propagation is done to simulate the effects of far-field wave propagation and scattering. Such wave propagation depends upon propagation distance (e.g. Δ or θ) in a highly oscillatory manner. This facilitates the asymptotic evaluation of travelling wave sums by isolating the most rapidly varying part of the frequency and spatial dependence. It also means that the resulting theory is restricted to the case where the distances between source and scatterers as well as between the scatterers and the receiver are of the order of about one wavelength or greater.

4.1 Spectrum of tapered seismograms

For the response of a given component (e.g. vertical, radial, or transverse) consider the displacements projected onto a polarization direction $\hat{\mathbf{p}}$. We wish to evaluate the time integral of the product of $\hat{\mathbf{p}}\cdot\mathbf{u}_0(\mathbf{r},t)$ or $\hat{\mathbf{p}}\cdot\mathbf{u}(\mathbf{r},t)$ and a suitable taper function $g(t)$. From eq. (11) we are led to consider the convolutions over frequency

$$\begin{aligned} C_{\oplus}(\mathbf{r},\omega) &= \frac{1}{2\pi}\,[\hat{\mathbf{p}}\cdot\mathbf{u}_0(\mathbf{r},\omega)] * G(\omega) \\ C_{\oplus+\delta\oplus}(\mathbf{r},\omega) &= \frac{1}{2\pi}\,[\hat{\mathbf{p}}\cdot\mathbf{u}(\mathbf{r},\omega)] * G(\omega). \end{aligned} \tag{25}$$

These convolutions may be evaluated starting with eqs (14) and (19) for the laterally homogeneous case and eqs (19), (21) and (24) for the laterally heterogeneous case.

4.2 Asymptotic evaluation of travelling wave sums

All expressions embodied in eqs (25), when considered term by term, depend on Hankel functions or, in the case of the evaluation of ψ_n in eq. (24), on a product of Hankel functions. The asymptotic expression for the Hankel functions in the limit of large wavenumber or distance is (Abramowitz & Stegun 1972)

$$H_m^{(2)}(\nu\Delta) = \sqrt{\frac{2}{\pi\nu\Delta}}\exp\left[-i\left(\nu\Delta - \frac{\pi}{2}m - \frac{\pi}{4}\right)\right] \quad (\nu\Delta \gg 1). \tag{26}$$

From this expression it follows that the evaluations of $C_{\oplus}$ and $C_{\oplus+\delta\oplus}$ will involve integrals over ω of highly oscillatory functions $\exp(-i\,\nu(\omega)\Delta)$ multiplied by smoothly varying functions of ω. Moreover, spatial gradients of the Hankel functions, which appear in the expressions for $\psi_n^0(\hat{\mathbf{r}},\omega)$ and $\psi_n(\hat{\mathbf{r}},\omega)$, contribute mainly through a leading term involving only spatial gradients of the same exponential functions. These considerations allow us to approximate $C_{\oplus}$ and $C_{\oplus+\delta\oplus}$ with

$$\begin{aligned} C_{\oplus} &\simeq \frac{1}{2\pi}\hat{\mathbf{p}}\cdot\sum_n \left\{[U_n(r)\hat{\mathbf{r}} + V_n\nabla_1]\left[\psi_n^0(\hat{\mathbf{r}},\omega) * G(\omega)\right]\right. \\ &\quad \left. + [-W_n(r)\hat{\mathbf{r}}\times\nabla_1]\left[\psi_n^0(\hat{\mathbf{r}},\omega) * G(\omega)\right]\right\} \\ C_{\oplus+\delta\oplus} &\simeq \frac{1}{2\pi}\hat{\mathbf{p}}\cdot\sum_n \{[U_n(r)\hat{\mathbf{r}} + V_n\nabla_1]\,[\psi_n(\hat{\mathbf{r}},\omega) * G(\omega)] \\ &\quad + [-W_n(r)\hat{\mathbf{r}}\times\nabla_1]\,[\psi_n(\hat{\mathbf{r}},\omega) * G(\omega)]\}\,. \end{aligned} \tag{27}$$

The convolutions of the potential functions that appear in eq. (27) may, in turn, be approximated with

$$\begin{aligned} \psi_n^0(\hat{\mathbf{r}},\omega) * G(\omega) \simeq -\frac{\pi i}{2}\frac{\nu_n c_n}{U_n}(\nu_n/2\pi)^{\frac{1}{2}}\left(\frac{\Delta}{\sin\Delta}\right)^{\frac{1}{2}} \\ \times\left\{\Sigma_1\left[H_0^{(2)}(\nu_n(\omega)\Delta) * G(\omega)\right] + (\Sigma_2 - \Sigma_4)\left[H_1^{(2)}(\nu_n(\omega)\Delta) * G(\omega)\right]\right. \\ \left. + (\Sigma_3 - \Sigma_5)\left[H_2^{(2)}(\nu_n(\omega)\Delta) * G(\omega)\right]\right\}, \end{aligned} \tag{28}$$

$$\begin{aligned} \psi_n(\hat{\mathbf{r}},\omega) * G(\omega) \simeq \psi_n^0(\hat{\mathbf{r}},\omega) * G(\omega) + \frac{i}{4c_n U_n}\sum_{n'}\int\left(\frac{\theta}{\sin\theta}\right)^{\frac{1}{2}} \\ \times\sum_{m=0}^{2}(-\nu_n)^m\,\delta\omega_{nn'}^{(m)}(\hat{\mathbf{r}}')\left\{\left[H_m^{(2)}(\nu_n(\omega)\theta)(\sqrt{2}H_+)^m\psi_{n'}^0(\hat{\mathbf{r}}',\omega)\right] * G(\omega)\right\} d^2\hat{\mathbf{r}}'. \end{aligned} \tag{29}$$

In the neighbourhood of ω, the wavenumber $\nu_n(\omega)$ may be expanded in a Taylor's series:

$$\nu_n(\omega') = \nu_n(\omega) + \left.\frac{\partial \nu_n}{\partial \omega}\right|_\omega (\omega' - \omega) + \frac{1}{2}\left.\frac{\partial^2 \nu_n}{\partial \omega^2}\right|_\omega (\omega' - \omega)^2 + \cdots. \tag{30}$$

Eqs (26) and (30) allow us to make the further approximations

$$H_m^{(2)}(\nu_n(\omega)\Delta) * G(\omega) \simeq H_m^{(2)}(\nu_n(\omega)\Delta) \int_{-\infty}^{\infty} \exp\left\{ i \left[\left(\left.\frac{\partial \nu_n}{\partial \omega}\right|_\omega \Delta \right) \omega' - \frac{1}{2}\left(\left.\frac{\partial^2 \nu_n}{\partial \omega^2}\right|_\omega \Delta \right) \omega'^2 \right] \right\} G(\omega')\, d\omega', \tag{31}$$

$$\begin{aligned} \left[H_m^{(2)}(\nu_n(\omega)\theta)(\sqrt{2}H_+)^m \psi_{n'}^0(\hat{\mathbf{r}}', \omega)\right] * G(\omega) &\simeq H_m^{(2)}(\nu_n(\omega)\theta)(\sqrt{2}H_+)^m \psi_{n'}^0(\hat{\mathbf{r}}', \omega) \\ &\times \int_{-\infty}^{\infty} \exp\left\{ i \left[\left(\left.\frac{\partial \nu_n'}{\partial \omega}\right|_\omega \Delta + \left.\frac{\partial \nu_n}{\partial \omega}\right|_\omega \theta \right) \omega' - \frac{1}{2}\left(\left.\frac{\partial^2 \nu_n'}{\partial \omega^2}\right|_\omega \Delta + \left.\frac{\partial^2 \nu_n}{\partial \omega^2}\right|_\omega \theta \right) \omega'^2 \right] \right\} \\ &\times G(\omega')\, d\omega'. \end{aligned} \tag{32}$$

Note that the use of the asymptotic expression for the Hankel functions in eq. (26) is a good approximation of the exact response function (it is proportional to the travelling wave Legendre function $Q_{\nu-\frac{1}{2}}^{m(1)}(\cos\theta)$ defined in Appendix B of Dahlen & Tromp 1998) at 'far-field' distances of about one wavelength or greater from the source or the scatterer. The resulting expression for the convolved total wavefield potential, that is eq. (29), implicitly includes both forward and backward scattering effects.

4.3 Waveform isolation with Hanning function

Up to this point we are liberty to choose any taper function $g(t)$ which would localize the desired waveform into a suitable time window. We choose to work with a Hanning function centred on a target body-wave arrival time t_0 with a half-width Δt:

$$g(t) = a(t - t_0, \Delta t), \tag{33}$$

where the Hanning function $a(t, \Delta t)$ is defined by eq. (A2). Since

$$G(\omega) = \exp(-i\omega t_0) A(\omega, \Delta t), \tag{34}$$

with $A(\omega, \Delta t)$ given by eq. (A3), eq. (31) becomes

$$\begin{aligned} H_m^{(2)}(\nu_n(\omega)\Delta) * G(\omega) &\simeq H_m^{(2)}(\nu_n(\omega)\Delta)\xi(\beta_n, \alpha_n, \Delta t) \\ \beta_n &= \left.\frac{\partial \nu_n}{\partial \omega}\right|_\omega \Delta - t_0, \quad \alpha_n = -\frac{1}{2}\left(\left.\frac{\partial^2 \nu_n}{\partial \omega^2}\right|_\omega \Delta \right), \end{aligned} \tag{35}$$

and eq. (32) becomes

$$\begin{aligned} [H_m^{(2)}(\nu_n(\omega)\theta)(\sqrt{2}H_+)^m \psi_{n'}^0(\hat{\mathbf{r}}', \omega)] * G(\omega) &\simeq [H_m^{(2)}(\nu_n(\omega)\theta)(\sqrt{2}H_+)^m \psi_{n'}^0(\hat{\mathbf{r}}', \omega)] \\ &\times \xi(\beta_{n'n}, \alpha_{n'n}, \Delta t) \\ \beta_{n'n} = \left.\frac{\partial \nu_n'}{\partial \omega}\right|_\omega \Delta + \left.\frac{\partial \nu_n}{\partial \omega}\right|_\omega \theta - t_0, &\quad \alpha_{n'n} = -\frac{1}{2}\left(\left.\frac{\partial^2 \nu_n'}{\partial \omega^2}\right|_\omega \Delta + \left.\frac{\partial^2 \nu_n}{\partial \omega^2}\right|_\omega \theta \right), \end{aligned} \tag{36}$$

where the *interaction function* $\xi(\beta, \alpha, \Delta t)$ is given by eq. (A16). Eqs (28) and (29) are then approximated by

$$\begin{aligned} \psi_n^0(\hat{\mathbf{r}}, \omega) * G(\omega) \simeq -\frac{\pi i}{2} \frac{\nu_n c_n}{U_n} (\nu_n/2\pi)^{\frac{1}{2}} \left(\frac{\Delta}{\sin\Delta}\right)^{\frac{1}{2}} \\ \times \left\{ \Sigma_1 H_0^{(2)}(\nu_n(\omega)\Delta) + (\Sigma_2 - \Sigma_4) H_1^{(2)}(\nu_n(\omega)\Delta) \right. \\ \left. + (\Sigma_3 - \Sigma_5) H_2^{(2)}(\nu_n(\omega)\Delta) \right\} \xi(\beta_n, \alpha_n, \Delta t), \end{aligned} \tag{37}$$

$$\begin{aligned} \psi_n(\hat{\mathbf{r}}, \omega) * G(\omega) \simeq \psi_n^0(\hat{\mathbf{r}}, \omega) * G(\omega) + \frac{i}{4 c_n U_n} \sum_{n'} \int \left(\frac{\theta}{\sin\theta}\right)^{\frac{1}{2}} \\ \times \sum_{m=0}^{2} (-\nu_n)^m\, \delta\omega_{nn'}^{(m)}(\hat{\mathbf{r}}') \left[H_m^{(2)}(\nu_n(\omega)\theta)(\sqrt{2}H_+)^m \psi_{n'}^0(\hat{\mathbf{r}}', \omega) \right] \\ \times \xi(\beta_{n'n}, \alpha_{n'n}, \Delta t)\, d^2\hat{\mathbf{r}}'. \end{aligned} \tag{38}$$

Substitution of the convolutions expressed by eqs (37) and (38) into eq. (27) provides semi-analytic estimates of $C_\oplus$ and $C_{\oplus+\delta\oplus}$ that depend only on the source–receiver geometry, scattering geometry and the inverse group velocities $\frac{\partial \nu_n}{\partial \omega}$ and their derivatives $\frac{\partial^2 \nu_n}{\partial \omega^2}$ at angular frequency ω. In the scattered wavefield, the interaction between different modes n and n' is expressed spatially through the interaction kernels $\delta\omega_{nn'}^{(m)}(\hat{\mathbf{r}}')$ and the Hankel functions, and temporally through the interaction function $\xi(\beta_{n'n}, \alpha_{n'n}, \Delta t)$. Note that $\beta_{n'n}$ defined in eq. (36) has the

physical interpretation of being the reduced traveltime of the wavegroup generated by incident dispersion branch n' propagating with group velocity $1/(\partial \nu_{n'}/\partial\omega)$, and converted to scattered dispersion branch n propagating with group velocity $1/(\partial\ \nu_n/\partial\omega)$.

4.4 Interaction function

For a source–receiver distance of 2×10^{-2} rad (i.e. ~126 km) that would apply to a regional wave propagation problem, typical source-scatterer and scatterer–receiver distances are $\Delta \sim \theta \sim 10^{-2}$ rad. For wave propagation at 1 Hz ($\omega = 2\pi$ rad s^{-1}), typical values of group velocity and the derivative of group velocity with respect to ω are

$$\begin{aligned} U &= \frac{1}{\partial\nu/\partial\omega} \sim 5 \times 10^{-4}\,\mathrm{rad\,s^{-1}} \\ \left|\frac{\partial U}{\partial\omega}\right| &= \left|-U^2\left(\frac{\partial^2\nu}{\partial\omega^2}\right)\right| \sim 10^{-6}\text{–}10^{-3}\ \mathrm{rad}. \end{aligned} \tag{39}$$

This translates into values of α of

$$|\alpha| \sim \left|\frac{1}{2}\frac{\partial U/\partial\omega}{U^2}(\Delta+\theta)\right| \sim\ 0.04\text{–}40\,\mathrm{s^2}. \tag{40}$$

For a given α and Δt the interaction function $\xi(\beta, \alpha, \Delta t)$ is symmetric with respect to β and achieves a maximum amplitude at $\beta = 0$. Eq. (A21) shows that for small α, the width of the interaction function scales with Δt. It is apparent from eq. (A16) that for large α, the width of the function scales with $2\pi\alpha/\Delta t$. Fig. 2 shows examples of $\xi(\beta, \alpha, \Delta t)$ for $\Delta t = 2$ sec and various values of α. It is clear that the amplitude of the interaction function diminishes rapidly for $|\beta| \gtrsim \Delta t$ for small α, whereas the width is greater for large α. The width of the interaction function is a measure of how efficiently two dispersion branches will couple. If t_0 and Δt are properly chosen, then the reduced traveltime $B_{n'n}$ will lie within the central portion of $\xi(\beta, \alpha, \Delta t)$ for the desired phase and be well removed from $\beta = 0$ for other phases. In order to isolate, for example, the *S*-wave arrival, Δt should be small enough to capture little energy from the *S*–*S* wave, fundamental mode surface waves, etc., but large enough to capture the entire arriving *S* wave. Apart from the need to window enough of the signal, a choice of very small Δt is not sufficient to isolate a signal because, as noted above, the temporal scale of interactions is then governed by α with a $\sim 2\pi\alpha/\Delta t$ dependence.

4.5 Relative amplitude and traveltime shifts

The traveltime shift may be derived by maximizing a cross-correlation function of the form

$$C = \int [u_0(t)\, g(t)][u_1(t-\delta T)\, g(t-\delta T)]\, dt$$

$$u_1(t) = u_0(t) + \delta u(t), \tag{41}$$

where we have used the notation $u_0 = \hat{\mathbf{p}}\cdot\mathbf{u}_0$ and $\delta u = \hat{\mathbf{p}}\cdot(\mathbf{u}-\mathbf{u}_0)$. The steps in this derivation are given in earlier studies (e.g. Dahlen *et al.* 2000; Zhao *et al.* 2000); the cross-correlation function defined in eq. (41) differs from earlier treatments only in the appearance of the taper function $g(t)$. Maximization of C with respect to δT, retaining only first-order terms in δu and δT, yields

$$\delta T\ =\ \frac{\int_{-\infty}^{\infty}\omega^2|[u_0(\omega)*G(\omega)]|^2\delta T(\omega)\,d\omega}{\int_{-\infty}^{\infty}\omega^2|[u_0(\omega)*G(\omega)]|^2\,d\omega}, \tag{42}$$

where $\delta T\ (\omega)$ is a frequency-dependent traveltime perturbation given by

$$\delta T(\omega) = -\frac{1}{\omega}\mathrm{Im}\left\{\frac{[\delta u(\omega)*G(\omega)]}{[u_0(\omega)*G(\omega)]}\right\} = \frac{\mathrm{Re}\left\{i\omega\,[u_0(\omega)*G(\omega)]^*\ [\delta u(\omega)*G(\omega)]\right\}}{\omega^2|[u_0(\omega)*G(\omega)]|^2}. \tag{43}$$

The traveltime shift is positive for a phase delay (i.e. later arrival) and negative for a phase advance (i.e. early arrival). The corresponding amplitude perturbation is

$$\delta(\ln A)\ =\ \frac{\int_{-\infty}^{\infty}|[u_0(\omega)*G(\omega)]|^2\delta(\ln A)(\omega)\,d\omega}{\int_{-\infty}^{\infty}|[u_0(\omega)*G(\omega)]|^2\,d\omega}, \tag{44}$$

where $\delta(\ln\ A)\ (\omega)$ is a frequency-dependent relative amplitude perturbation given by

$$\delta(\ln A)(\omega) = \mathrm{Re}\left\{\frac{[\delta u(\omega)*G(\omega)]}{[u_0(\omega)*G(\omega)]}\right\} = \frac{\mathrm{Re}\,\{[u_0(\omega)*G(\omega)]^*\,[\delta u(\omega)*G(\omega)]\}}{|[u_0(\omega)*G(\omega)]|^2}. \tag{45}$$

From eqs (25), (43) and (45), the frequency-dependent relative amplitude and traveltime shifts resulting from the structural perturbations may be expressed as

$$\delta(\ln A)(\omega) = \mathrm{Re}\left\{\ln\left[\frac{C_{\oplus+\delta\oplus}(\mathbf{r},\omega)}{C_{\oplus}(\mathbf{r},\omega)}\right]\right\}, \tag{46}$$

$$\delta T(\omega) = -\frac{1}{\omega}\mathrm{Im}\left\{\ln\left[\frac{C_{\oplus+\delta\oplus}(\mathbf{r},\omega)}{C_{\oplus}(\mathbf{r},\omega)}\right]\right\}. \tag{47}$$

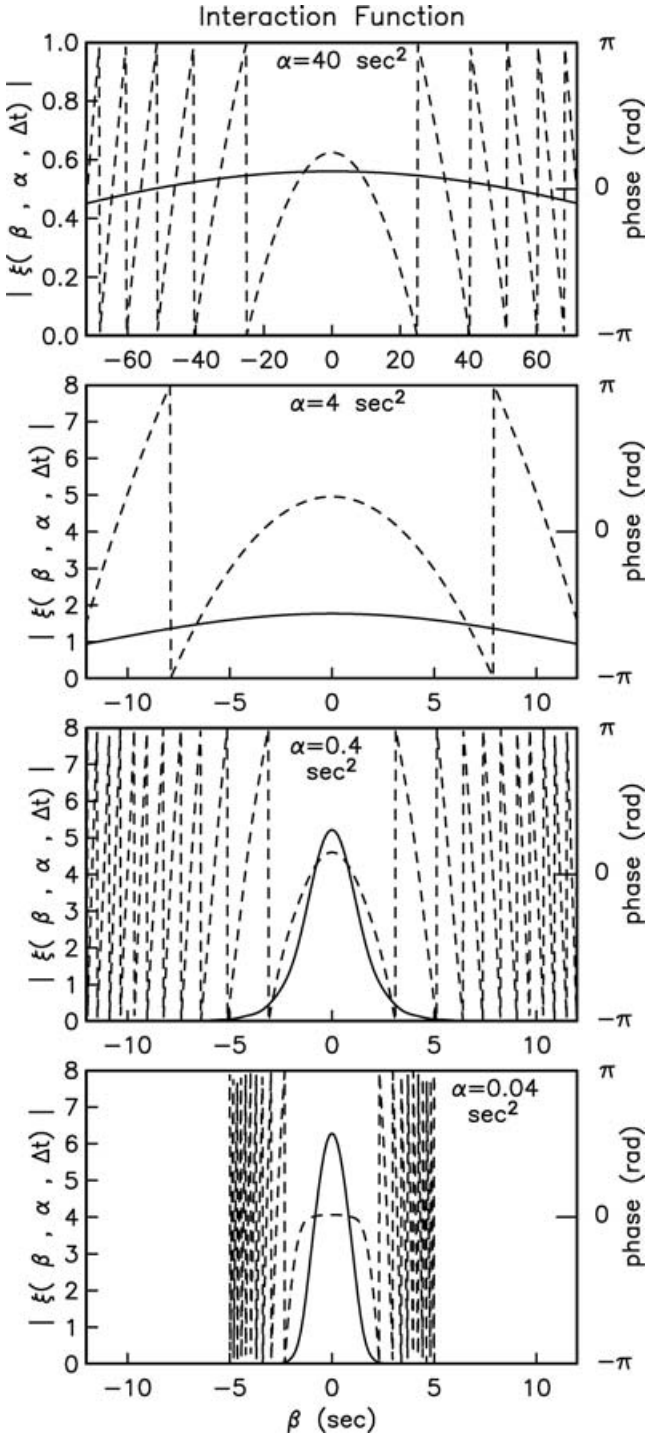

Figure 2. Interaction function $\xi(\beta, \alpha, \Delta t)$ for $\Delta t = 2$ s depicted in terms of its amplitude and phase, for four typical values of α. For $\alpha = 0.04$ s^2 the phase is omitted in the extremely low-amplitude areas ($|\beta| > 5$ s).

Eq. (42) is equivalent to eq. 66 of Dahlen *et al.* (2000) for the special case of $g(t)$ being a boxcar function defined over the desired time interval. It is clear that for a narrow-window signal with dominant frequency ω, δT in eq. (42) would be well approximated by δT (ω). As noted by Zhao *et al.* (2000) the use of frequency-dependent relative amplitude and traveltime shifts, such as defined by eqs (46) and (47), is more general and affords the potential advantage of extracting frequency-dependent information in isolated wave trains.

Note that the definition of ξ in eq. (A1) shows that a range of frequencies about the target frequency ω contributes to the interaction function and hence to δT (ω) and $\delta(\ln A)$ (ω). If we use a dummy frequency variable ω' in eq. (A1), the frequency range over which the integrand factor A (ω', Δt) is large is roughly the Nyquist frequency of the target window $\omega_{\rm Nyq} = \pi/\Delta t$, which is typically a large fraction of ω if Δt is just large enough to capture a few cycles. For coupling between dispersion branches with a small associated α, the integration

involved in evaluating ξ is then over the fullest possible range of frequencies, that is, a range of half-width $\sim\omega_{\rm Nyq}$. In this case, eq. (A21) and Fig. 2 show that the interaction function is sharply peaked near $\beta = 0$, diminishing to negligible values for $|\beta| > \Delta t$. This limits the spatial range of significant perturbations to be for relatively small β, which translates into a cone enveloping the direct ray path of width of at most a few Fresnel zones. It is essentially the cancelling behaviour among the contributions of many frequencies in the evaluation of ξ that produces a spatially limited region of scattered signals with similar arrival time as that of the direct arrival.

5 EXAMPLES OF SENSITIVITY KERNELS FOR CRUSTAL WAVE PROPAGATION

For wave propagation through a relatively simple layered structure, that of a constant vertical velocity gradient, predicted sensitivity kernels from the coupled travelling wave approach agree well with those predicted from geometrical ray theory (Appendix B). Such a structure possesses an upper discontinuity at Earth's surface but no internal or lower discontinuities, greatly reducing potential interference effects among different body waves. In the following, we consider a more realistic stratification that includes internal crustal discontinuities as well as the Mohorovičić discontinuity

We consider wave propagation at angular frequency $\omega = 2\pi$ rad s^{-1} through the isotropic earth structure shown in Fig. 3, which has a crustal thickness of 25 km. Wave velocities and density are specified to a depth of 150 km, at which a zero-displacement boundary condition is applied. This is a locked-mode approximation (Nolet *et al.* 1989), and it is useful because it reduces the number of mode branches associated with propagating waves. It yields accurate results provided that seismograms are evaluated at times shorter than the arrival time of the first reflections from this artificial boundary. For Rayleigh waves there are 108 mode branches with horizontal phase velocity less than 100 km s^{-1} associated with propagating waves at this ω. There are also an infinite number of mode branches associated with non-propagating waves (Pollitz 2001). (More precisely, there are an infinite number of mode branches, each of them associated with wavenumbers that are

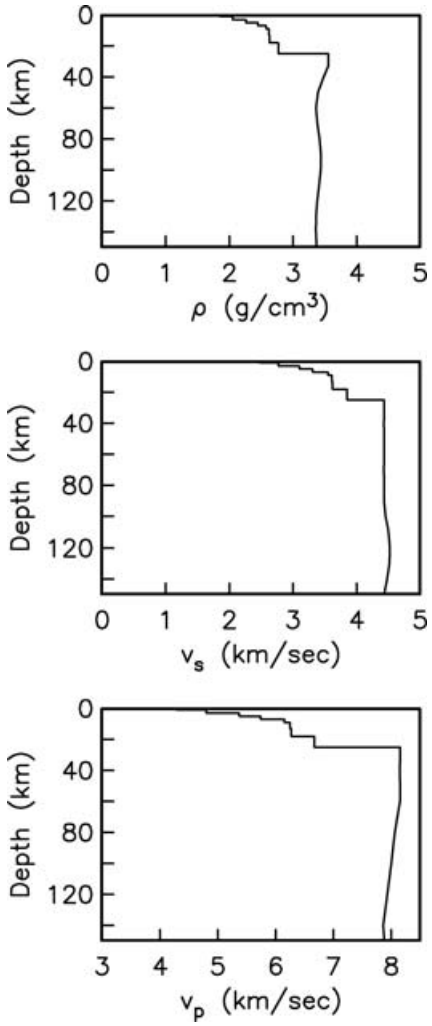

Figure 3. Layered crustal model Wald *et al.* (1991) underlain by a layered mantle prescribed by continental Model 7 of Nolet (1977) down to 150 km depth. We specify shear attenuation parameter $Q_\mu = 300$ below 5 km depth, $Q_\mu = 100$ above 5 km depth, and bulk attenuation parameter $Q_\kappa = 2.5 \times Q_\mu$.

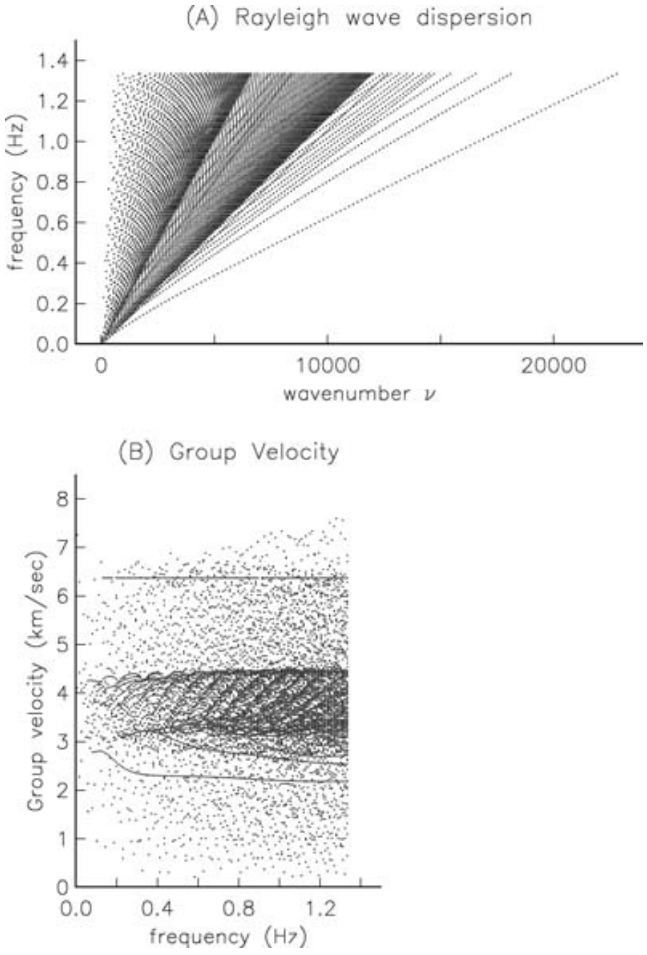

Figure 4. (a) Dispersion and (b) group velocity of travelling waves on the layered earth model shown in Fig. 3, subject to a locked mode approximation (see text). There are altogether 9295 travelling waves at the 125 angular frequencies shown.

fully complex or purely real. For a given frequency, only a finite number of these mode branches have propagating waves associated with real-valued wavenumber.)

To put the efficiency of the approach into perspective, diagrams of travelling wave dispersion and corresponding group velocity at 125 discrete frequencies from 0 to 1.333 Hz are shown in Fig. 4. If eqs (28) and (29) were used to synthesize the convolutions with spherically symmetric potentials $\psi_n^0(\hat{\mathbf{r}}, \omega) * G(\omega)$ and first-order wavefield potentials $\psi_n(\hat{\mathbf{r}}, \omega) * G(\omega)$ without further simplification (using a numerical integration with all angular frequencies), then all 9295 travelling waves depicted in Fig. 4 would need to be synthesized. The forms of these convolutions in eqs (37) and (38), in which the frequency integral contained in the convolution operations has been evaluated at a single angular frequency via the interaction function, reduces the problem to a synthesis of travelling waves at the target frequency, of which there are only 108.

5.1 1 Hz wave propagation through the crust

To illustrate the complexity of wave propagation through the crust, synthetic wavefields are generated on the laterally homogeneous model. We place a point source at depth 11.9 km with non-trivial moment tensor components $M_{\theta\theta} = -M_{\phi\phi}$, where $\hat{\theta}$ and $\hat{\phi}$ point due South and East, respectively. This source generates maximal *P–SV* wave energy towards azimuths of 0°, 90°, 180° and 270°. The wavefields are evaluated in the time domain using the inverse Fourier transform of eq. (14), with all travelling waves up to a maximum horizontal phase velocity of 100 km s^{-1}, and low-pass filtered at 1.333 Hz with a corner period at 0.667 Hz. Fig. 6 shows snapshots of the resulting wavefield along a south-trending profile. A number of body-wave phases may be identified, of which the *S* and *sS* phases are the most prominent. Both *S* and *SmS* (*S* reflected off the Mohorovičić discontinuity) propagate through the volume, and both *S*-wave phases can be followed coherently. Note that until the maximum horizontal offset of 83.9 km on the plots, the *sS* wave does not yet turn and thus would never produce a separate arrival at any hypothetical receiver at the surface. However, as shown in the next section the *sS* wave proves to have a large influence on the resulting sensitivity kernels for the arriving *S* wave.

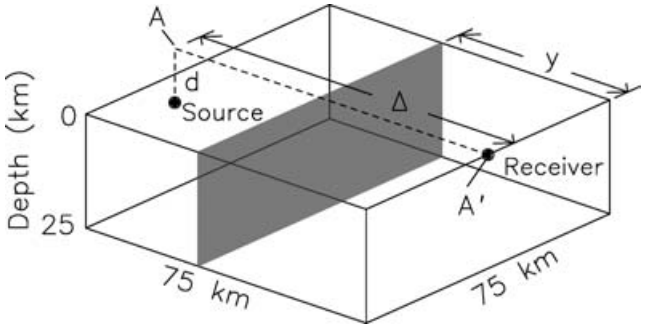

Figure 5. Source–receiver configuration for synthetic calculations. Δ and d are the source–receiver angular distance and source depth, respectively. The shaded plane represents a profile, at distance y from the receiver, along which traveltime and amplitude sensitivity kernels are calculated.

5.2 *S*-wave propagation at subcritical offset

A source is placed at depth $d = 11.9$ km and a receiver at the Earth's surface at distance $\Delta = 1.316 \times 10^{-2}$ rad $= 83.9$ km south of the epicentre (Fig. 5). We assign a point source with non-trivial moment tensor components $M_{\theta\theta} = -M_{\phi\phi}$. The source–receiver azimuth is 0°, that is, along one of the four maximal lobes for *P–SV* wave excitation. For purpose of illustration we consider only Rayleigh wave propagation and neglect mode coupling with Love waves.

For the given source and receiver positions, the predicted arrival times of the *S*, *SmS*, and *sP* waves are 25.1, 25.6 and 18.8 s, respectively. Ray paths and traveltime curves for these waves are shown in Figs 7(a) and (b). As discerned in Fig. 6, the *S* wave turns just above the mantle and propagates coherently throughout the crust until its arrival at the receiver.

Eqs (27), (37), (38), (46) and (47) collectively prescribe the relationships given in eqs (4) and (5), that is, sensitivity kernels $K_\mu^{(\delta T)}(\omega; \mathbf{r}, \mathbf{r}')$, $K_\kappa^{(\delta T)}(\omega\,; \mathbf{r}, \mathbf{r}')$, and $K_\rho^{(\delta T)}(\omega; \mathbf{r}, \mathbf{r}')$ for traveltime shift, and similarly for the amplitude shift. In order to estimate the sensitivity kernels for the *SV* wave, we use $\hat{\mathbf{p}} = \hat{\mathbf{r}}$ for the polarization direction, assign $t_0 = 25.1$ s, and $\Delta t = 2$ s. The 4-s-wide time window applied to isolate the body wave phase and calculate the spectra of the Hanning-tapered arrival is shown in Fig. 8(a). At a target point $\mathbf{r}'$ we specify a small scatterer $\delta\oplus$ consisting of a perturbation $\delta\mu$ in a volume $V = 2.68$ km^3 centred on $\mathbf{r}'$. Scaling relationships $\delta\rho/\rho = 0.17 \times (\delta\mu/\mu)$ and $\delta\kappa/\kappa = 0.33 \times (\delta\mu/\mu)$ are used to specify perturbations in other parameters. The resulting traveltime shift at a receiver $\mathbf{r}$ is thus a linear combination of $K_\mu^{(\delta T)}(\omega; \mathbf{r}, \mathbf{r}')$, $K_\kappa^{(\delta T)}(\omega; \mathbf{r}, \mathbf{r}')$, and $K_\rho^{(\delta T)}(\omega; \mathbf{r}, \mathbf{r}')$, and similarly for the amplitude shift. For brevity, we denote the overall perturbation with a velocity perturbation $\delta v\ (\mathbf{r}')$ and refer to the resultant traveltime and amplitude shifts as (e.g. eqs 6 and 7)

$$\delta T = K_{\delta v}^{(\delta T)}(\omega; \mathbf{r}, \mathbf{r}')\, \delta v(\mathbf{r}')\, V$$

$$\delta(\ln A) = K_{\delta v}^{(\delta(\ln A))}(\omega; \mathbf{r}, \mathbf{r}')\, \delta v(\mathbf{r}')\, V.$$

Depending on depth, $\delta\mu$ is chosen such that the resulting perturbation in shear wave velocity $v = \sqrt{\mu/\rho}$ is $\delta v/v = +12$ per cent.

Figs 9(a) and 10(a), (b) show slices of sensitivity kernels using mode coupling among all 108 travelling wave branches. Figs 9(b) and 10(c), (d) shows them with mode coupling restricted to the first 15 travelling wave branches, that is, the fundamental mode plus 14 higher mode branches. There are substantial differences between the two sets of images, with Figs 10(c), (d) giving the appearance of containing scattering effects mainly near the *S*-wave unperturbed ray path and Figs 10(a), (b) suggesting interference effects with other wave types. The *sS* wave is a substantial source of interference in the sensitivity kernels, since many pronounced interfering signals in Fig. 9(a) and Figs 10(a), (b) track the high-amplitude *sS* path. In order to produce scattered waves arriving at the same time as the direct *S* wave, *sS* must convert into a phase travelling faster than the *S* wave speed. The converted waves must be either surface waves, which travel with wave speed between the *S* and *P* wave speeds, or *P* waves. In the latter case it is straightforward to visualize the interference. Fig. 11 shows the traveltime of the $sS \rightarrow$ P scattered arrival relative to direct *S*, as a function of position of the scatterer. Substantial interference is expected when the difference in traveltime is 2 s or less (i.e. the two arrivals are within a time Δt of one another). The $sS \rightarrow$ P interference is potentially most severe at $\gtrsim$45 km distance from the source. The efficiency of *sSarrow*P conversion varies little as a function of scattering angle in the volume of interest, and the interference effects exhibited at distances >45 km from the source in Fig. 9(a) correlate well with the band of predicted $sS \rightarrow$ P scattered arrivals at these distances (Fig. 11).

Why is the *sS* interference largely absent in Figs 9(b) and 10(c), (d)? This is understood by relating the horizontal phase velocity c of a particular travelling wave branch to the ray parameter p (e.g. Aki & Richards 1980):

$$c = \frac{\omega}{\nu} = \frac{1}{p}. \tag{48}$$

The suite of rays contributing to a scattered body-wave arrival will correspond to ray parameters at bottoming depths within one or two Fresnel zones of the direct ray path. That is, letting $v\ (r_b) = 1/p$ be the wave speed at the radius r_b where the ray path turns, ν will be in the range $\omega/v\ (r)$ for r distributed about r_b. For the direct *S*-wave arrival in the above example, $p = 0.2696$ s km^{-1} (1718 s rad^{-1}) and $\nu = \omega p$ is 10780. This is approximately the wavenumber of the 5th highest mode. To synthesize the direct *S*-wave arrival for the given source–receiver configuration thus requires inclusion of several travelling wave branches with wavenumbers distributed about 10780. The ray parameter of the high-amplitude *sS* waves in the volume between source and receiver (Fig. 6) varies from about 0.20 s km^{-1} at shallow depths to 0.24 s km^{-1}

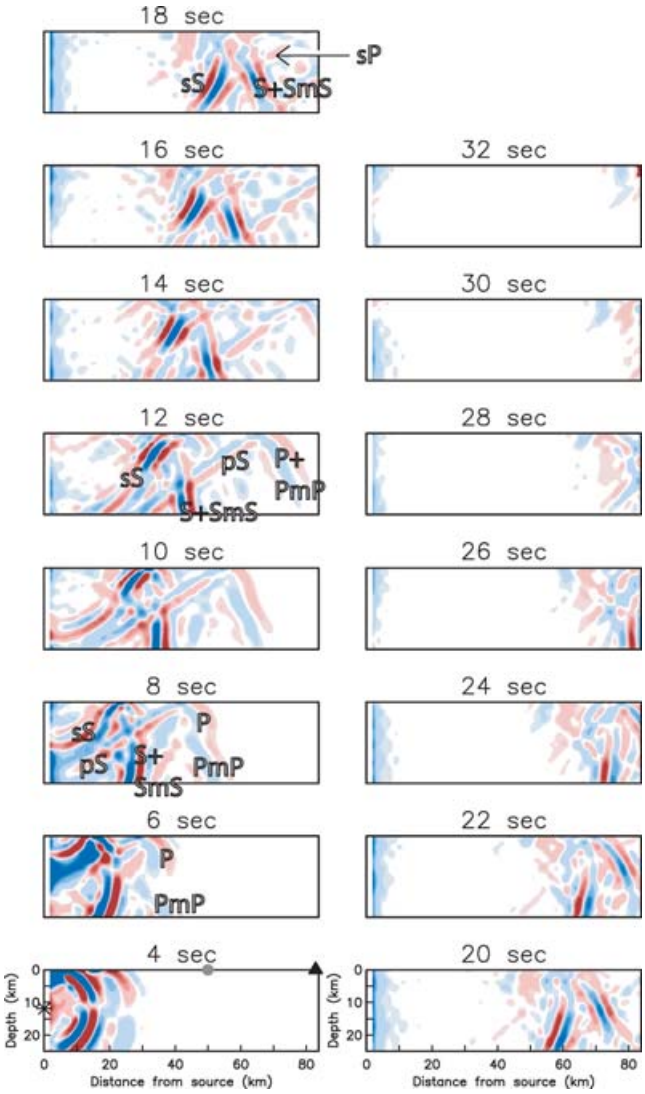

Figure 6. Snapshots of vertical-component synthetic wavefields on the laterally homogeneous model (Fig. 3) low-pass filtered at 1.333 Hz with a corner period at 0.667 Hz. A point source at depth 11.9 km is indicated by $*$, and the receivers considered in Sections 5.2 and 5.4 are indicated by a triangle and circle, respectively. For the point source the non-trivial elements of the moment tensor are $M_{\theta\theta} = -M_{\phi\phi}$, and the profile is along the direction of increasing θ, that is, one of the four lobes of maximal *P–SV* wave excitation.

at greater depths, corresponding to a range $\nu \sim 8000$–9600; 8000 is approximately the dimensionless wavenumber of the 36th highest mode, and 9600 is approximately the dimensionless wavenumber of the 9th highest mode. Restriction to the 15 highest mode branches retains the *S* wave and partially removes the influence of scattering from *sS* and other high-angle surface reflections, which are associated with relatively small p and hence small wavenumbers ν. Since the ninth highest mode is retained in Figs 10(c), (d), one expects a certain amount of remaining interference arising at least from interaction of *sS* with near-surface structure.

We further test the influence of low wavenumbers on the resulting sensitivity kernels by restricting the dispersion branches to those associated with $c \leq 8$ km s^{-1}, which is satisfied for the highest 66 mode branches. In this and subsequent examples, we find negligible difference between these sensitivity kernels and those generated using all dispersion branches up to $c = 100$ km s^{-1}. This verifies that the scattering interactions investigated under the considered source–receiver configurations are effectively restricted to propagation through the crust, that is, the upper 25 km.

5.3 *S*-wave propagation at post-critical offset

A post-critical *S* wave may be generated by placing the source relatively deep or assigning a relatively large source–receiver offset. We choose to keep the offset $\Delta = 1.316 \times 10^{-2}$ rad as in the previous section, but increase the source depth to $d = 20$ km. In this case there is at short wavelength no downgoing *S* wave which arrives at the receiver, only an upgoing *S* wave with initially very shallow initial incidence angle (Fig. 7c). The theoretical *S*-wave and *SmS*-wave arrival times are 24.4 and 24.8 s, respectively, and the associated slownesses are

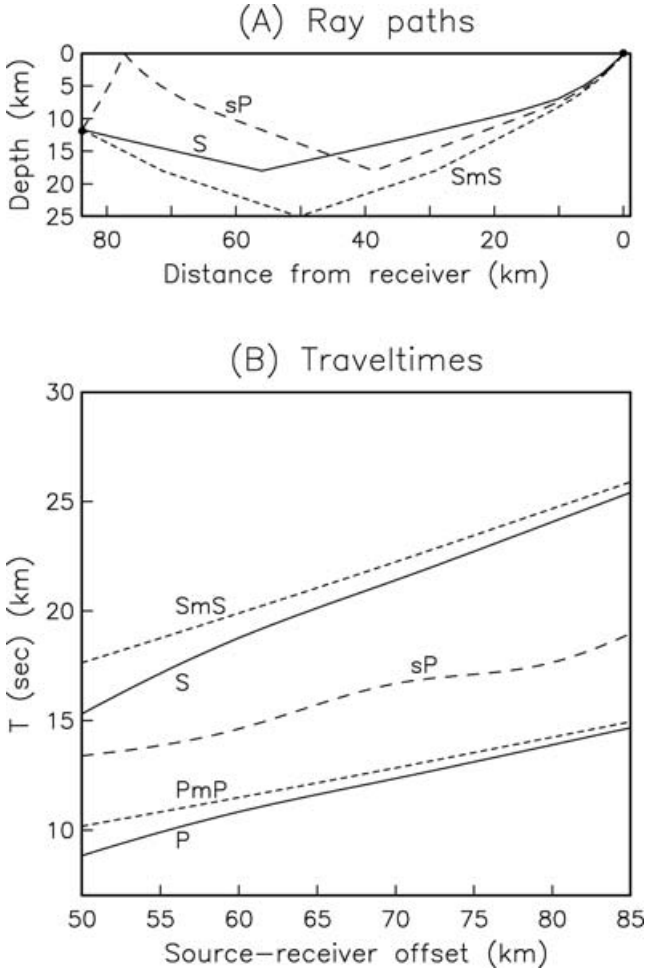

Figure 7. (a) Various ray paths generated by a source at depth $d = 11.9$ km and source–receiver offset of 1.316×10^{-2} rad (83.9 km). (b) Traveltime versus source–receiver offset for $d = 11.9$ km. Note that the *P* ray path is identical to the *S* ray path (and the *PmP* ray path identical to the *SmS* ray path) because Poisson's ratio is constant (=0.25) in the crust. (c) Various ray paths generated by a source at depth $d = 20$ km and source–receiver offset of 1.316×10^{-2} rad (83.9 km). (d) Traveltime versus source–receiver offset for $d = 20$ km.

0.2596 s km^{-1} for the *S* wave and 0.2526 s km^{-1} for the *SmS* wave. At finite wavelength the *S* wave train is coherent throughout its propagation path in the crust (Fig. 12), with continuity between turning *S* waves and the wide-angle reflection *SmS* off the Mohorovičić discontinuity. Targeting the wide-angle *S*-wave reflection *SmS*, we use $t_0 = 24.8$ s and $\Delta t = 2$ s (Fig. 8b). Taking all 108 mode branches results in the sensitivity kernels shown in Figs 9(c) and 10(e), (f). The corresponding result using just the 15 highest mode branches is shown in Figs 9(d) and 10(g), (h). The scattered $sS \rightarrow$ P waves are, as before, of similar traveltime as the direct *SmS* wave over a large volume, with dominant interference predicted to arise from relatively deep scatterers. However, Figs 10(e) and (f) exhibit subdued interference effects compared with the case of subcritical offset. The reduced interference effects in this case are judged to arise from the large amplitude of wide-angle *S* relative to that of *sS* (Fig. 12), resulting in less complicated sensitivity kernels compared with the case of subcritical offset. Those obtained with the 15 highest mode branches see sensitivity distributed near the unperturbed *SmS* ray path (Figs 9d and 10g, h), with very little sensitivity to near-surface structure because of the suppression of wave conversions involving steeply incident waves.

5.4 *P*-wave propagation

The case of propagation of the direct *P* wave is simpler than *S*-wave propagation because the possibilities of interference from other wave types is minimized since the *P* wave speed is much faster than the *S* wave speed. As an example, we use $\Delta = 7.848 \times 10^{-3}$ rad s^{-1} (50 km), $d = 11.9$ km and assign a source with non-trivial moment tensor components $M_{rr} = M_{\theta\theta} = M_{\phi\phi}$. The direct *P* wave has arrival time 8.85 s and ray parameter $p = 0.1593$ s km^{-1}, which corresponds to $\nu = 6377$ for the direct ray path. With the choices of $\delta\mu$ and the scaling relationships used in previous sections, the change in compressional wave velocity $v = \sqrt{(\kappa + 4/3\mu)/\rho}$ is $\delta v/v = +5.4$ per cent; this perturbation is applied within a volume $V = 2.68$ km^3 centred on the scatterer. Figs 9(e) and 10(i), (j) shows the sensitivity kernels obtained using the 17 mode branches associated with dimensionless wave numbers from 5154 to 6904, $t_0 = 8.85$ s and $\Delta t = 2$ s (Fig. 8c). The traveltime kernels maintain a doughnut-like appearance seen in simpler examples (e.g. Hung *et al.* 2000) despite the propagation through a series of mid-crustal

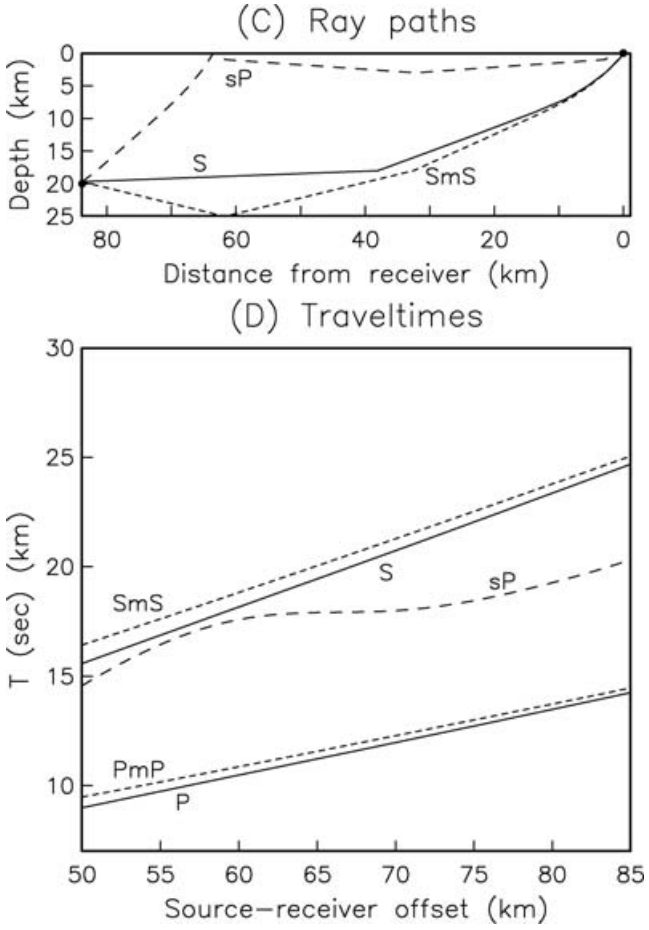

Figure 7. (*Continued*.)

discontinuities (Fig. 3) as well as the fact that the wavelength ∼5–6 km is comparable with the distance to the free surface. Fig. 9(e) also demonstrates sensitivity to backscattering over a certain distance behind the source, which arises because the back-scattered energy can arrive within the time window of interest. Some interference is contributed by the *PmP* wave which arrives about 1.34 s after direct *P* (Fig. 7b). The *PmP* wave can be distinguished from the *P* wave in the wavefield snapshots at times earlier than about 8 s (Fig. 6), but they merge into one composite wave at times greater than about 12 s. In this example the *PmP* wave arrives with relatively small amplitude near the end of the time window (Fig. 8c). Its ray parameter is 0.1261 s km^{-1}, corresponding to a dimensionless wavenumber of 5048. This lies just outside the range of dimensionless wavenumbers used to synthesize the sensitivity kernels, thereby reducing its influence.

6 DISCUSSION

The synthetic traveltime and amplitude perturbations explored in the previous section demonstrate that for crustal wave propagation, it is generally difficult to completely isolate the sensitivity kernels $K_{\delta v}^{(\delta T)}$ of a particular wave type from sensitivity to other waves. This is established based on both inspection of traveltime curves for a particular source–receiver configuration as well comparisons between sensitivities obtained with and without relatively steeply incident waves, for example, those with horizontal phase velocity greater than about 4.5 km s^{-1}. This gives rise to generally complicated $K_{\delta v}^{(\delta T)}$ even for an *S* wave which is well isolated in the unperturbed seismogram. The predominant interfering phase encountered in the present examples is the *sS* wave, which may scatter into a *P* wave over a wide range of depths, or into surface waves travelling with horizontal phase velocity between that of the *S*-wave and *P*-wave speeds. Under other circumstances (e.g. shorter source–receiver offsets), reflections from the Mohorovičić discontinuity could contribute further interference. Interference effects arise both because different wave types may arrive at the same time and because the Fresnel-zone width of a 1 Hz body wave at propagation distances of a few tens of km is a modest fraction of the crustal thickness.

The rule of zero sensitivity of traveltime to perturbations located on the centre of the ray path is well established theoretically for direct and isolated *P* or *S* arrivals subject to geometrical ray theory (e.g. Yomogida 1992; Woodward 1992; Dahlen *et al.* 2000; Zhao *et al.* 2000). Similarly there is theoretically maximal sensitivity to perturbations located on the centre of the ray path for rays that have touched one caustic (or an odd number of caustics). The numerical examples with *S* waves presented here do not obviously conform to either rule. This is partly because of the strong effect of the source radiation pattern, which corresponds to strike slip along a vertical fault and which therefore

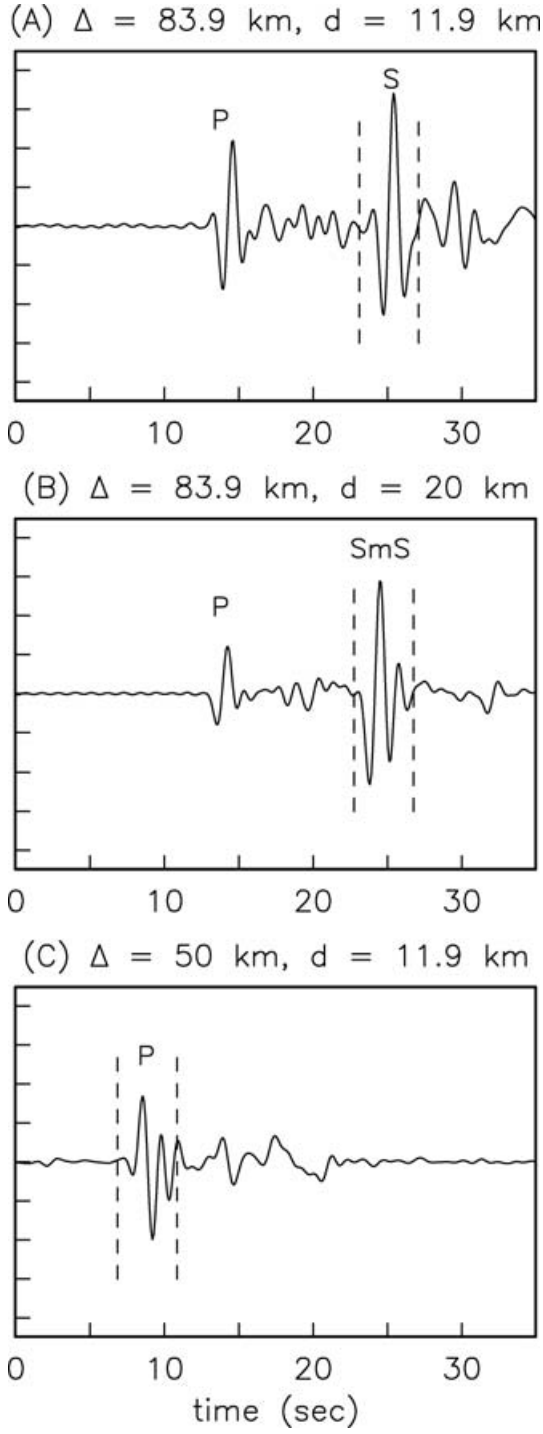

Figure 8. Vertical-component synthetic seismograms on the laterally homogeneous model (Fig. 3) low-pass filtered at 1.333 Hz with a corner period at 0.667 Hz, at various source–receiver offsets and source depths. The seismograms are calculated using the travelling wave representation of eq. (14). For each point source, the non-trivial elements of the moment tensor are $M_{\theta\theta} = -M_{\phi\phi}$ in (a) and (b) and $M_{rr} = M_{\theta\theta} = M_{\phi\phi}$ in (c). Dashed lines indicate the time window of half-width $\Delta t = 2$ s used for the Hanning taper to derive spectra of the tapered body wave arrivals.

suppresses *SV* wave excitation in the horizontal direction. The foregoing sensitivity patterns thus tend to miss the upper part of the doughnut which starts along a horizontal propagation path (incidence angle 90°), the lower part of the doughnut being more complete because its path starts with an incidence angle somewhat less than 90°. This is illustrated by examining the sensitivity kernels generated with a non-trivial moment tensor component $M_{r\theta}$. This source generates maximal *P–SV* wave energy along azimuths of 0° and 180° and along initial incidence angle of 90°. Fig. 13 shows the sensitivity kernels for a source–receiver offset of 83.9 km and various values of source depth d. In each case the time window of width $\Delta t = 2$ s is centred on the arrival time of direct *S*. The sensitivity kernels are relatively doughnut-like for source depths ranging from about 6 and 12 km. Shallower sources generate waves that interact with the free surface, and deeper sources generate waves

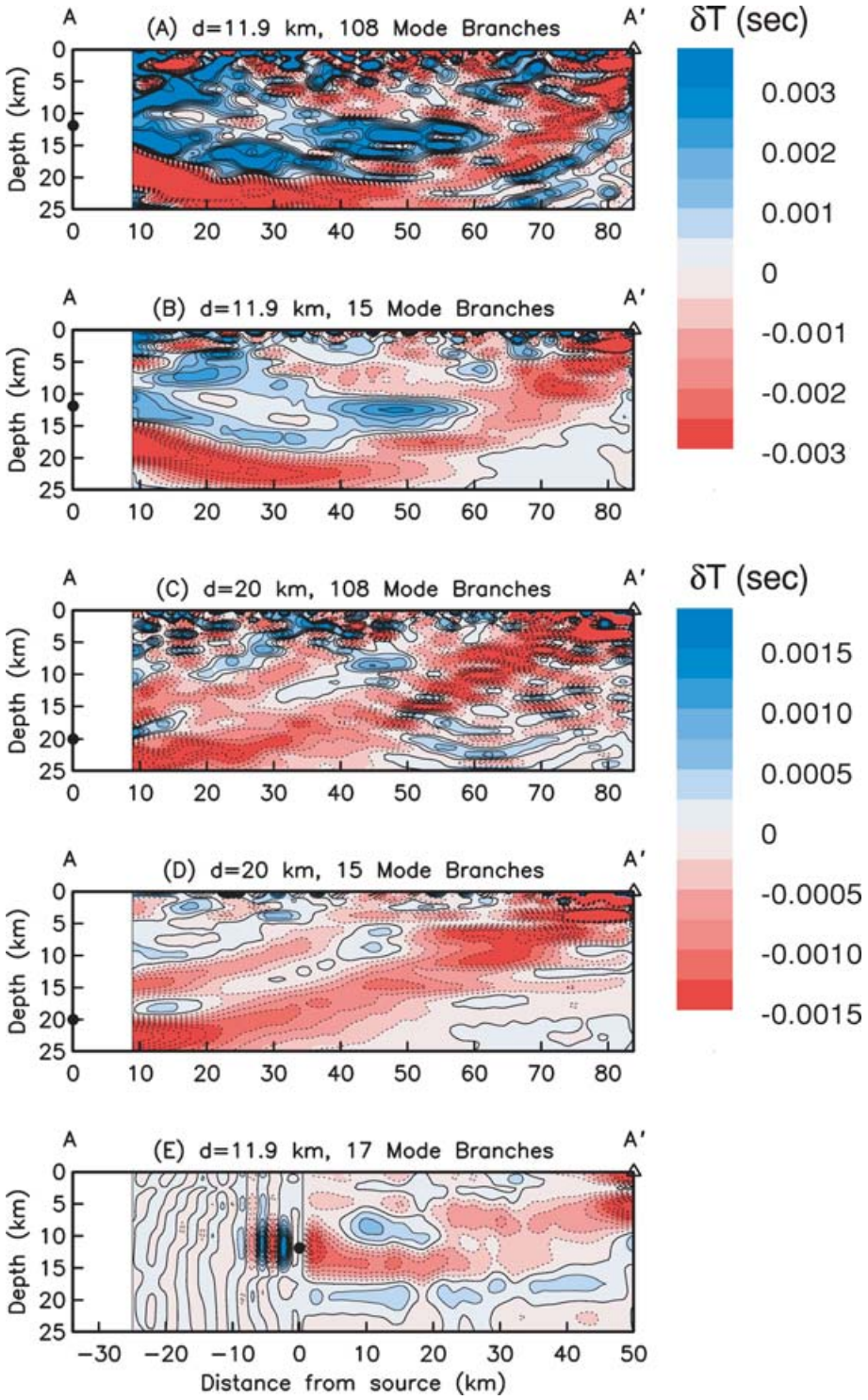

Figure 9. Sensitivity kernels for traveltime ($\delta T = K_{\delta v}^{(\delta T)} \delta v V$) on a vertical plane containing the source and receiver (AA' shown in Fig. 5) for the configurations corresponding to (a) Figs 10(a and b), (b) Figs 10(c and d), (c) Figs 10(e and f), (d) Figs 10(g and h) and (e) Figs 10(i and j). In each plot the source is indicated by a filled circle and the receiver by a triangle. Note a difference in scale between parts (a) and (b) versus parts (c) to (e).

that interact with the Moho, in both cases disrupting the doughnut pattern. Comparison of Fig. 9(b) with Fig. 13(f), and similarly Fig. 9(d) with Fig. 13(j), shows that the source mechanism exerts a substantial influence on the traveltime sensitivity kernels through its control over the radiation pattern.

The influence of interfering phases complicates the use of $K_{\delta v}^{(\delta T)}$ for use in regional tomography. The complications described here for a 1-D reference model are even more severe for a 3-D reference model (Zhao *et al.* 2005). If the relative phases and amplitudes of the target wave and the interfering wave(s) were well known, then the composite $K_{\delta v}^{(\delta T)}$ would be approximately representative of the true kernels. In practice,

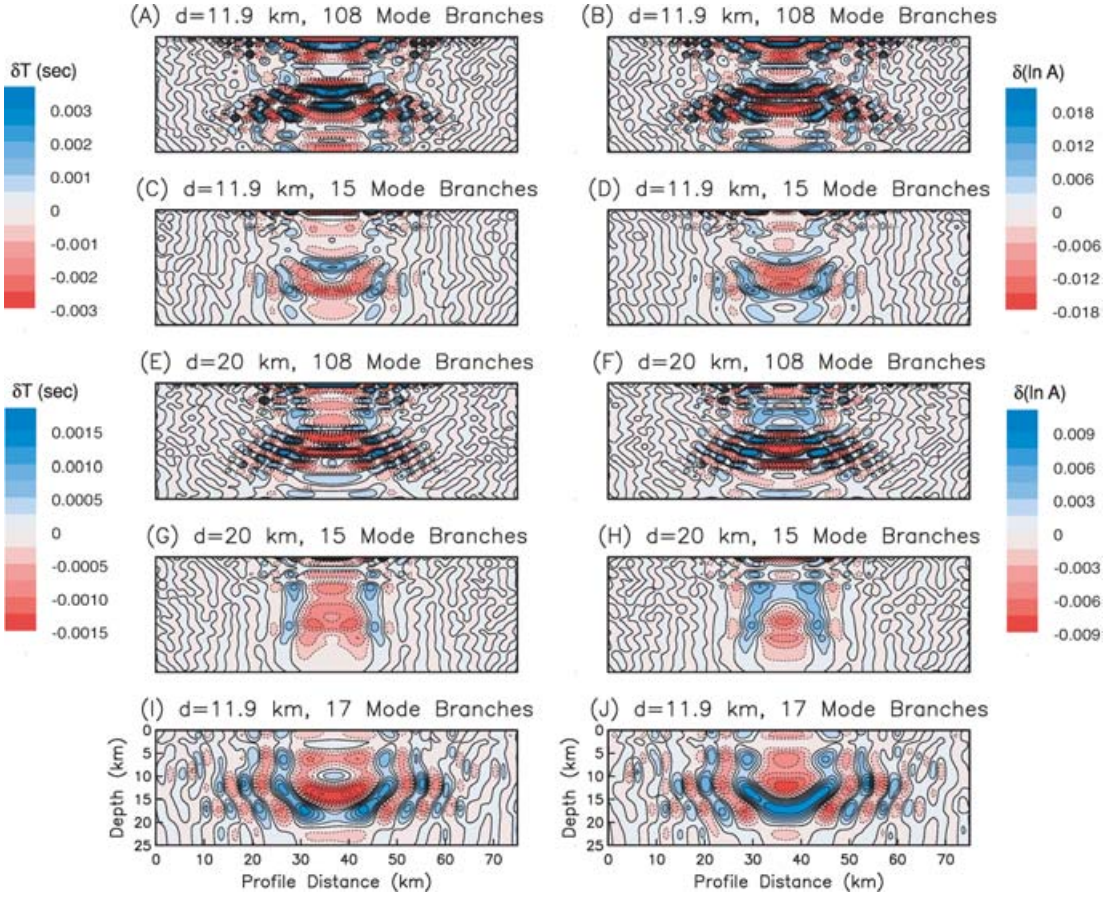

Figure 10. Sensitivity kernels for traveltime (a, c, e, g, i) ($\delta T = K_{\delta v}^{(\delta T)}\,\delta v V$) and amplitude (b, d, f, h, j) ($\delta(\ln A) = K_{\delta v}^{(\delta(\ln A))}\,\delta v V$) for the *SV* wave (parts a - h) or *P* wave (parts i and j) for a configuration with source depth d, source–receiver distance 83.9 km, and coupling among the given number of mode branches. The vertical slice corresponds to the profile distance $y = 30$ km in Fig. 5. Note the difference in traveltime scale in parts (a), (c) versus parts (e), (g), (i); similarly for the amplitude scale in parts (b), (d) versus parts (f), (h), (j).

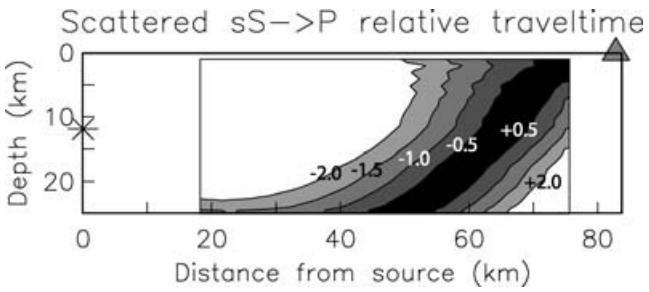

Figure 11. $sS \rightarrow$ P traveltime relative to the direct *S*-wave traveltime as a function of scattering position, for the given source–receiver configuration (source indicated by $*$, the receiver by a triangle at 83.9 km horizontal offset). Numerals are the relative traveltime in sec.

this is unlikely to be the case, and the obtained composite $K_{\delta v}^{(\delta T)}$ are better regarded as a superposition of the sensitivity of the desired wave type plus 'noise' consisting of the contributions of interfering phases. The interference effects are less severe for *P*-wave propagation because of its high wave speed, hence reduced interference from waves propagating with the *S* wave speed. For a regional tomography experiment, Fig. 7 suggests that separation among body wave arrivals is generally maximized (i.e. interference minimized) for sources placed in the mid-upper crust and for relatively small source–receiver offsets. Very shallow sources generate stronger interference from free-surface reflections, and likewise for deep sources interacting with the Mohorovičić discontinuity.

For analysis of a large data set of crustal *S*- and *P*-wave traveltimes (and possibly amplitudes), for purpose of speed of computation it would be preferable to use those $K_{\delta v}^{(\delta T)}$ computed from a restricted set of mode branches, for example, restricted to the neighbourhood of wavenumber ν that corresponds to the target ray path via eq. (48). This is sufficient to capture scattering effects generated by the desired wave type, but, depending on source depth, it will not capture the scattering arising from reflections off the free surface or Mohorovičić

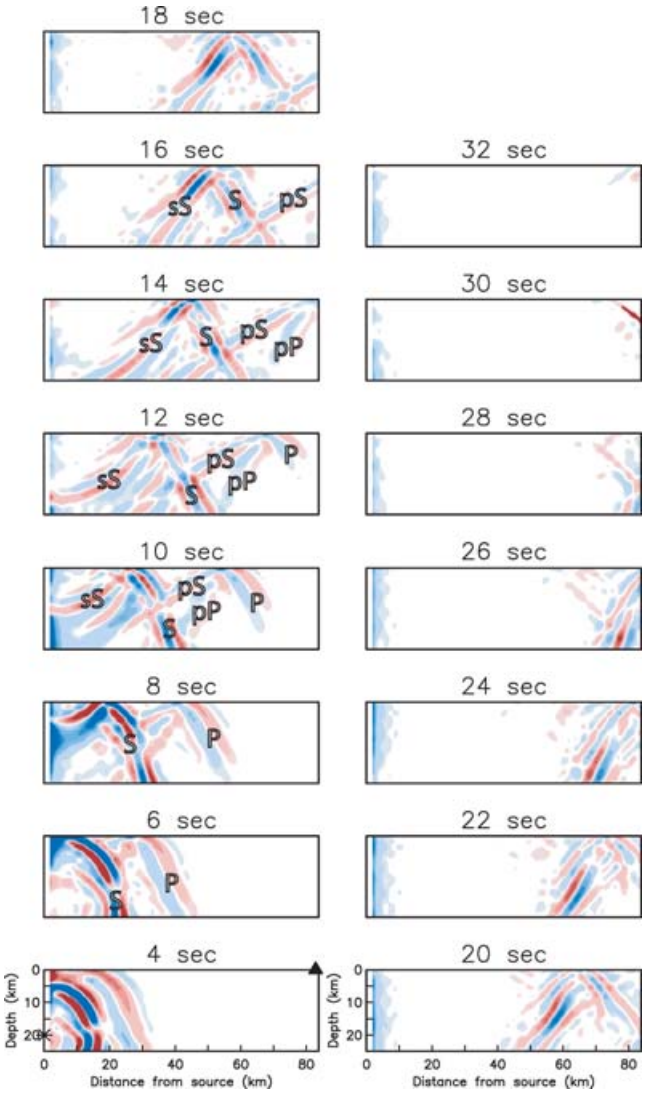

Figure 12. Snapshots of vertical-component synthetic wavefields on the laterally homogeneous model (Fig. 3) low-pass filtered at 1.333 Hz with a corner period at 0.667 Hz. A point source at depth 20 km is indicated by $*$, and the receiver considered in Section 5.3 is indicated by a triangle. For the point source the non-trivial elements of the moment tensor are $M_{\theta\theta} = -M_{\phi\phi}$ (i.e. strike slip on a vertical fault), and the profile is along the direction of increasing θ, that is, one of the four lobes of maximal *P–SV* wave excitation.

discontinuity generated by relatively steeply incident waves. This procedure is attractive not only because of the computational savings (the computation time is proportional to the square of the number of mode branches) but also because the wave interactions involving more steeply incident waves are usually a source of interference which cannot be precisely modelled. Even with a restricted set of mode branches, remaining non-geometrical wave effects (e.g. contributions to traveltime perturbations from conversion to surface waves at the free surface) may provide useful constraints on structural perturbations. This depends upon the extent to which the reference model is adequate for representing the true structure. We suggest that this is more likely to be the case for non-geometrical effects generated near the receiver, where the relative phases of the target wave and additional waves may be predictable.

7 CONCLUSIONS

We apply seismic travelling wave coupling theory to the evaluation of relative amplitude and traveltime shifts of isolated body waves. By making use of a Taylor's series expansion of wavenumber along a dispersion branch as a function of frequency, we obtain semi-analytic expressions for frequency-dependent sensitivity kernels of traveltime and amplitude. We give examples of sensitivity kernels for 1 Hz wave propagation through the crust. Sensitivity kernels for crustal wave propagation are generally complicated because the Fresnel zone width is typically of the same order as the source depth (leading to first-order non-geometrical interactions with the free surface) and/or the difference between the source depth and Moho depth. For a target body wave, this generally leads to interference from body wave reflections from the free surface and/or Moho as well as surface waves.

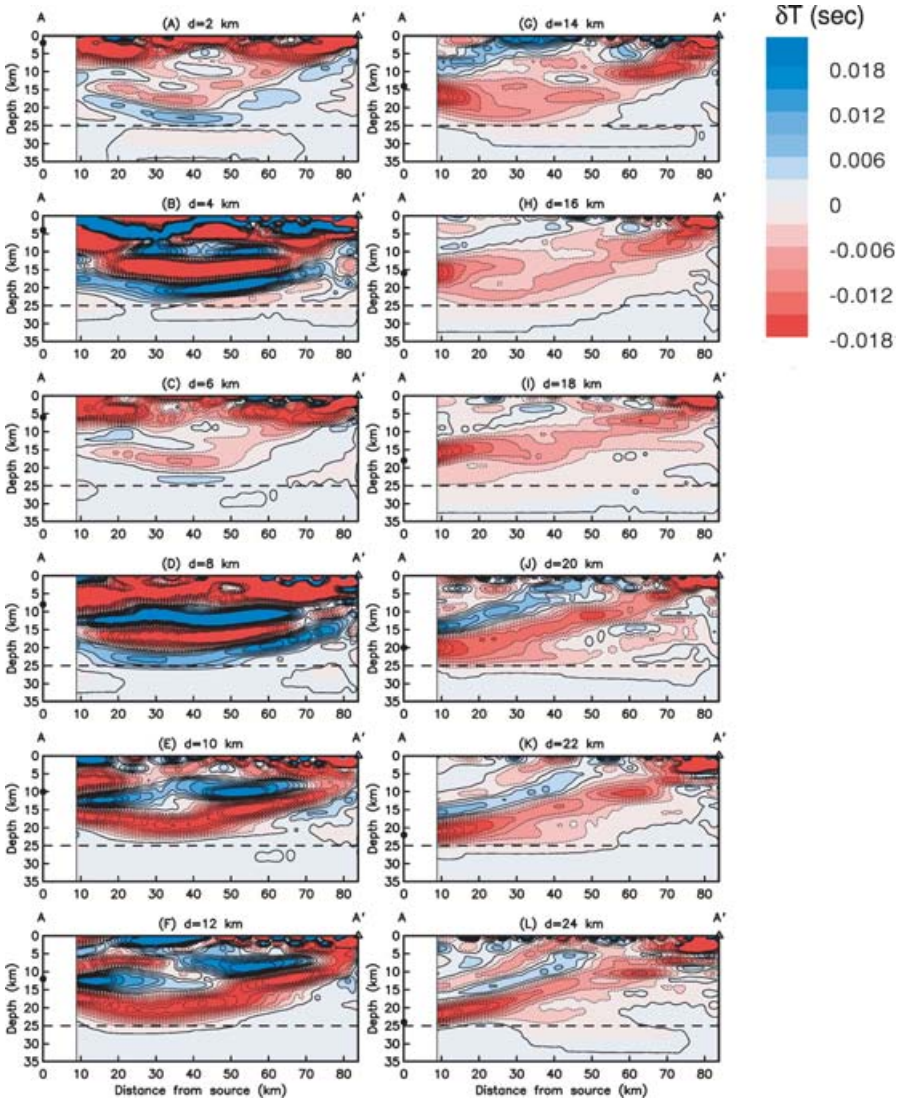

Figure 13. Sensitivity kernels for *S*-wave traveltime ($\delta T = K_{\delta v}^{(\delta T)} \delta v V$) on a vertical plane containing the source and receiver (AA' shown in Fig. 5) with indicated source depth d, source–receiver distance 83.9 km, and coupling among the highest 15 dispersion branches. The source radiation pattern is generated with a non-trivial moment tensor component $M_{r\theta}$. In each plot the source is indicated by a filled circle and the receiver by a triangle.

The present treatment is designed for the calculation of sensitivity kernels relative to a spherically symmetric reference model. Recent numerical treatments are aimed at the calculation of sensitivity kernels relative to a 3-D reference model (e.g. Zhao *et al.* 2005; Liu & Tromp 2006). We anticipate that the framework presented here can be extended to the case of a 3-D reference structure by introducing scattering Greens functions that contain all necessary information for generating the scattered wavefield between all scatteres and a fixed set of receivers. This approach has been exploited using the finite difference method (Zhao *et al.* 2005) and spectral element method (Liu & Tromp 2006), and we anticipate that it is feasible with the coupled travelling wave approach.

ACKNOWLEDGMENTS

This paper has benefited from the critical comments of two anonymous reviewers and internal reviews by Joe Fletcher and Walter Mooney.

REFERENCES

Abramowitz, M. & Stegun, I., 1972. *Handbook of Mathematical Functions*, vol. 1, U.S. Dept. Commerce, National Bureau of Standards, Washington, DC.

Aki, K. & Richards, P., 1980. *Quantitative Seismology*, Vol. 1, W.H. Freeman and Company, San Francisco, California.

Baig, A., Dahlen, F. & Hung, S.-H., 2003. Traveltimes of waves in random 3-D media, *Geophys. J. Int.,* **153,** 1–16.

Dahlen, F., 1980. A uniformly valid asymptotic representation of normal multiplet spectra on a laterally heterogeneous Earth, *Geophys. J. R. Astr. Soc.,* **62,** 225–247.

Dahlen, F. & Tromp, J., 1998. *Theoretical Global Seismology*, Princeton University Press, Princeton, New Jersey.

Dahlen, F., Hung, S.-H. & Nolet, G., 2000. Fréchet kernels for finite-frequency traveltimes-I. Theory, *Geophys. J. Int.,* **141,** 157–174.

Friederich, W., 1999. Propagation of seismic shear and surface waves in a laterally heterogeneous mantle by multiple forward scattering, *Geophys. J. Int.,* **136,** 180–204.
Hudson, J., 1980. *The excitation and propagation of elastic waves*, Cambridge Univ. Press, Cambridge.
Hung, S.-H., Dahlen, F. & Nolet, G., 2000. Fréchet kernels for finite-frequency traveltimes-II. Examples, *Geophys. J. Int.,* **141,** 175–203.
Liu, Q.-Y. & Tromp, J., 2006. Finite-frequency kernels based upon adjoint methods, *Bull. seism. Soc. Am.*, submitted.
Marquering, H., Dahlen, F. & Nolet, G., 1999. The body-wave travel-time paradox: bananas, doughnuts and 3-D delay-time kernels, *Geophys. J. Int.,* **137,** 805–815.
Nolet, G., 1977. The upper mantle under Western Europe inferred from the dispersion of Rayleigh modes, *J. Geophys.,* **43,** 265–286.
Nolet, G., Sleeman, R., Nijhof, V. & Kennett, B., 1989. Synthetic reflection seismograms in three dimensions by a locked mode approximation, *Geophysics,* **54,** 350–358.
Pollitz, F., 1994. Surface wave scattering from sharp lateral discontinuities, *J. geophys. Res.,* **99,** 21 891–21 909.
Pollitz, F., 1998. Scattering of spherical elastic waves from a small-volume spherical inclusion, *Geophys. J. Int.,* **134,** 390–408.
Pollitz, F., 2001. Remarks on the travelling wave decomposition, *Geophys. J. Int.,* **144,** 233–246.
Romanowicz, B., 1987. Multiplet-multiplet coupling due to lateral heterogeneity: asymptotic effects on the amplitude and frequency of the Earth's normal modes, *Geophys. J. R. astr. Soc.,* **90,** 75–100.
Snieder, R. & Romanowicz, B., 1988. A new formalism for the effect of lateral heterogeneity on normal modes and surface waves, I: isotropic perturbations, perturbations of interfaces and gravitational perturbations, *Geophys. J. R. astr. Soc.,* **92,** 207–222.
Wald, D., Helmberger, D. & Heaton, T., 1991. Rupture model of the 1989 Loma Prieta earthquake from the inversion of strong-ground motion and broadband teleseismic data, *Bull. seism. Soc. Am.,* **81,** 1540–1572.
Woodward, M., 1992. Wave-equation tomography, *Geophysics,* **57,** 15–26.
Yomogida, K., 1992. Fresnel zone inversion for lateral heterogeneities in the Earth, *Pure appl. Geophys.,* **138,** 391–406.
Yomogida, K. & Aki, K., 1987. Amplitude and phase data inversion for phase velocity anomalies in the Pacific Ocean Basin, *Geophys. J. R. astr. Soc.,* **88,** 161–204.
Zhao, L., Jordan, T. & Chapman, C., 2000. Three-dimensional Fréchet differential kernels for seismic delay times, *Geophys. J. Int.,* **141,** 558–576.
Zhao, L., Jordan, T., Olsen, K. & Chen, P., 2005. Fréchet kernels for imaging regional earth structure based on three-dimensional reference models, *Bull. seism. Soc, Am.,* **141,** 2066–2080.

APPENDIX A: EVALUATION OF INTERACTION FUNCTION

Here we evaluate the *interaction function* given by the integral

$$\xi(\beta, \alpha, \Delta t) = \int_{-\infty}^{\infty} \exp[i(\beta\omega + \alpha\omega^2)]\, A(\omega, \Delta t)\, d\omega, \tag{A1}$$

for real-valued β and α, where

$$a(t, \Delta t) = \begin{cases} \frac{1}{2}\left(1 + \cos\frac{\pi t}{\Delta t}\right) & \text{for} |t| < \Delta t \\ 0 & \text{for} |t| \geq \Delta t x \end{cases} \tag{A2}$$

with Fourier transform

$$A(\omega, \Delta t) = \mathcal{F}[a(t)]|_\omega = \frac{1}{2}\left\{ \frac{2\sin(\omega\Delta t)}{\omega} + \frac{\sin\left[\left(\frac{\pi}{\Delta t} - \omega\right)\Delta t\right]}{\frac{\pi}{\Delta t} - \omega} + \frac{\sin\left[\left(\frac{\pi}{\Delta t} + \omega\right)\Delta t\right]}{\frac{\pi}{\Delta t} + \omega} \right\}. \tag{A3}$$

Substituting eq. (A3) into eq. (A1) we evaluate eq. (A1) term by term, $\xi = \xi_1 + \xi_2 + \xi_3$ starting with

$$\xi_1(\beta, \alpha, \gamma) = \int_{-\infty}^{\infty} \exp[i(\beta\omega + \alpha\omega^2)]\, \frac{\sin(\omega\gamma)}{\omega}\, d\omega. \tag{A4}$$

We have $\xi_1(\beta, \alpha, 0) = 0$ and

$$\begin{aligned} \frac{\partial\xi_1}{\partial\gamma} &= \frac{1}{2}\int_{-\infty}^{\infty} \exp[i(\beta\omega + \alpha\omega^2)]\, [\exp(i\omega\gamma) + \exp(-i\omega\gamma)]\, d\omega \\ &= \frac{1}{2}\exp[-i(\beta+\gamma)^2/4\alpha] \int_{-\infty}^{\infty} \exp\left[i\alpha\left(\omega + \frac{\beta+\gamma}{2\alpha}\right)^2\right] d\omega \\ &\quad + \frac{1}{2}\exp[-i(\beta-\gamma)^2/4\alpha] \int_{-\infty}^{\infty} \exp\left[i\alpha\left(\omega + \frac{\beta-\gamma}{2\alpha}\right)^2\right] d\omega. \end{aligned} \tag{A5}$$

Using the fact that

$$\int_{-\infty}^{\infty} \exp(i\alpha\omega^2)\, d\omega = \sqrt{\frac{\pi}{\alpha}}\exp(i\pi/4), \tag{A6}$$

we have

$$\frac{\partial\xi_1}{\partial\gamma} = \frac{1}{2}\sqrt{\frac{\pi}{\alpha}}\exp(i\pi/4)\{\exp[-i(\beta+\gamma)^2/4\alpha] + \exp[-i(\beta-\gamma)^2/4\alpha]\}. \tag{A7}$$

This results in

$$\xi_1(\beta, \alpha, \Delta t) = \frac{1}{2}\sqrt{\frac{\pi}{\alpha}}\exp(i\pi/4)\int_0^{\Delta t} \{\exp[-i(\beta+\gamma)^2/4\alpha] + \exp[-i(\beta-\gamma)^2/4\alpha]\}\, d\gamma. \tag{A8}$$

We next consider

$$\xi_2(\beta,\alpha,\gamma)=\frac{1}{2}\int_{-\infty}^{\infty}\exp[i(\beta\omega+\alpha\omega^2)]\,\frac{\sin\left[(\frac{\pi}{\Delta t}-\omega)\gamma\right]}{\frac{\pi}{\Delta t}-\omega}\,d\omega. \tag{A9}$$

We have $\xi_2(\beta,\alpha,0)=0$ and

$$\begin{aligned}\frac{\partial\xi_2}{\partial\gamma}&=\frac{1}{4}\int_{-\infty}^{\infty}\left\{\exp[i(\beta-\gamma)\omega+i\alpha\omega^2)]\exp\left(\frac{i\pi\gamma}{\Delta t}\right)\right.\\&\quad\left.+\ \exp[i(\beta+\gamma)\omega+i\alpha\omega^2)]\exp\left(-\frac{i\pi\gamma}{\Delta t}\right)\right\}d\omega\\&=\frac{1}{4}\exp\left[-i(\beta+\gamma)^2/4\alpha\right]\exp\left(-\frac{i\pi\gamma}{\Delta t}\right)\int_{-\infty}^{\infty}\exp\left[i\alpha\left(\omega+\frac{\beta+\gamma}{2\alpha}\right)^2\right]d\omega\\&\quad+\frac{1}{4}\exp\left[-i(\beta-\gamma)^2/4\alpha\right]\exp\left(\frac{i\pi\gamma}{\Delta t}\right)\int_{-\infty}^{\infty}\exp\left[i\alpha\left(\omega+\frac{\beta-\gamma}{2\alpha}\right)^2\right]d\omega.\end{aligned} \tag{A10}$$

Making use of eq. (A6) we have

$$\begin{aligned}\frac{\partial\xi_2}{\partial\gamma}&=\frac{1}{4}\sqrt{\frac{\pi}{\alpha}}\exp(i\pi/4)\left\{\exp\left[-i(\beta+\gamma)^2/4\alpha\right]\exp\left(-\frac{i\pi\gamma}{\Delta t}\right)\right.\\&\quad\left.+\exp\left[-i(\beta-\gamma)^2/4\alpha\right]\exp\left(\frac{i\pi\gamma}{\Delta t}\right)\right\}.\end{aligned} \tag{A11}$$

This results in

$$\begin{aligned}\xi_2(\beta,\alpha,\Delta t)&=\frac{1}{4}\sqrt{\frac{\pi}{\alpha}}\exp(i\pi/4)\int_0^{\Delta t}\left\{\exp\left[-i(\beta+\gamma)^2/4\alpha\right]\exp\left(-\frac{i\pi\gamma}{\Delta t}\right)\right.\\&\quad\left.+\ \exp\left[-i(\beta-\gamma)^2/4\alpha\right]\exp\left(\frac{i\pi\gamma}{\Delta t}\right)\right\}d\gamma.\end{aligned} \tag{A12}$$

In similar fashion we find that

$$\begin{aligned}\xi_3(\beta,\alpha,\Delta t)&=\frac{1}{2}\int_{-\infty}^{\infty}\exp[i(\beta\omega+\alpha\omega^2)]\,\frac{\sin[(\frac{\pi}{\Delta t}+\omega)\Delta t]}{\frac{\pi}{\Delta t}+\omega}\,d\omega\\&=\frac{1}{4}\sqrt{\frac{\pi}{\alpha}}\exp(i\pi/4)\int_0^{\Delta t}\left\{\exp\left[-i(\beta+\gamma)^2/4\alpha\right]\exp\left(\frac{i\pi\gamma}{\Delta t}\right)\right.\\&\quad\left.+\exp\left[-i(\beta-\gamma)^2/4\alpha\right]\exp\left(-\frac{i\pi\gamma}{\Delta t}\right)\right\}d\gamma.\end{aligned} \tag{A13}$$

We note that

$$\begin{aligned}\exp\left[-i(\beta+\gamma)^2/4\alpha\right]\exp\left(\frac{\pm i\pi\gamma}{\Delta t}\right)&=\exp\left[-i\left(\beta\mp\frac{2\pi}{\Delta t}\alpha+\gamma\right)^2/4\alpha\right]\\&\quad\times\exp\left[i\left(\frac{\pi}{\Delta t}\right)^2\alpha\mp\frac{i\pi\beta}{\Delta t}\right],\end{aligned} \tag{A14}$$

$$\begin{aligned}\exp\left[-i(-\beta+\gamma)^2/4\alpha\right]\exp\left(\frac{\pm i\pi\gamma}{\Delta t}\right)&=\exp\left[-i\left(-\beta\mp\frac{2\pi}{\Delta t}\alpha+\gamma\right)^2/4\alpha\right]\\&\quad\times\exp\left[i\left(\frac{\pi}{\Delta t}\right)^2\alpha\pm\frac{i\pi\beta}{\Delta t}\right].\end{aligned} \tag{A15}$$

Putting together eqs (A8) and (A12)–(A15) we may summarize the total $\xi=\xi_1+\xi_2+\xi_3$ as

$$\begin{aligned}\xi(\beta,\alpha,\Delta t)&=2E(\beta,\alpha,\Delta t)+\exp\left[i\left(\frac{\pi}{\Delta t}\right)^2\alpha-\frac{i\pi\beta}{\Delta t}\right]\\&\times\left[E\left(-\beta+\frac{2\pi}{\Delta t}\alpha,\alpha,\Delta t\right)+E\left(\beta-\frac{2\pi}{\Delta t}\alpha,\alpha,\Delta t\right)\right]\\&\quad+2E\left(-\beta,\alpha,\Delta t\right)+\exp\left[i\left(\frac{\pi}{\Delta t}\right)^2\alpha+\frac{i\pi\beta}{\Delta t}\right]\\&\times\left[E\left(\beta+\frac{2\pi}{\Delta t}\alpha,\alpha,\Delta t\right)+E\left(-\beta-\frac{2\pi}{\Delta t}\alpha,\alpha,\Delta t\right)\right],\end{aligned} \tag{A16}$$

where

$$E(\beta, \alpha, \Delta t) = \frac{1}{4}\sqrt{\frac{\pi}{\alpha}} \exp(i\pi/4) \int_0^{\Delta t} \exp[-i(\beta+\gamma)^2/4\alpha]\, d\gamma. \tag{A17}$$

The function $E(\beta', \alpha, \Delta t)$ may be written in terms of error functions with complex argument. It is useful to identify three cases:

$$E(\beta', \alpha, \Delta t) = \begin{cases} \frac{1}{4}\pi\left[\mathrm{Erf}\left(\frac{\beta'+\Delta t}{c}\chi\right) - \mathrm{Erf}\left(\frac{\beta'}{c}\chi\right)\right] & \text{for } \beta' > 0 \\ \frac{1}{4}\pi\left[\mathrm{Erf}\left(-\frac{\beta'}{c}\chi\right) - \mathrm{Erf}\left(-\frac{\beta'+\Delta t}{c}\chi\right)\right] & \text{for } \beta' < 0,\ \beta'+\Delta t < 0, \\ \frac{1}{4}\pi\left[\mathrm{Erf}\left(-\frac{\beta'}{c}\chi\right) + \mathrm{Erf}\left(\frac{\beta'+\Delta t}{c}\chi\right)\right] & \text{for } \beta' < 0,\ \beta'+\Delta t > 0 \end{cases} \tag{A18}$$

where $c = 2\sqrt{\alpha}$ and $\chi = \exp(i\,\pi/4)$. This can be re-cast in terms of complex Fresnel integrals by using the relation (Abramowitz & Stegun 1972)

$$\mathrm{Erf}(\chi z) = \sqrt{2}\,\chi[C - iS]\left(\sqrt{\frac{2}{\pi}}z\right), \tag{A19}$$

where

$$C(z) = \int_0^z \cos\left(\frac{\pi}{2}\gamma^2\right) d\gamma, \quad S(z) = \int_0^z \sin\left(\frac{\pi}{2}\gamma^2\right) d\gamma. \tag{A20}$$

The limiting value of $\xi(\beta, \alpha, \Delta t)$ for small α is

$$\lim_{\alpha\to 0} \xi(\beta, \alpha, \Delta t) = 2\pi \mathcal{F}^{-1}[A(\omega, \Delta t)]|_{t=\beta} = 2\pi a(\beta, \Delta t). \tag{A21}$$

Since $\lim_{\Delta t\to\infty} A(\omega, \Delta t) = 2\pi\ \delta(\omega)$, the limiting value of $\xi(\beta, \alpha, \Delta t)$ for large Δt is

$$\lim_{\Delta t\to\infty} \xi(\beta, \alpha, \Delta t) = 2\pi. \tag{A22}$$

APPENDIX B: COMPARISON WITH GEOMETRICAL RAY THEORY

B1 Sensitivity kernels from geometrical ray theory

We apply geometrical ray theory to derive simple analytic expressions for the frequency-dependent traveltime and amplitude sensitivity kernels for a direct body-wave arrival, for example, the *SV* wave. The following closely parallels earlier treatments (Dahlen *et al.* 2000; Zhao *et al.* 2000) but differs slightly in the definitions of $\delta T(\omega)$ and $\delta(\ln A)\ (\omega)$. Narrow window behaviour is produced in all methods by appropriate averaging over frequency, and in the present method this is accomplished through isolating the desired signal with a taper function $G\ (\omega)$ and evaluating the convolutions over frequency given by eqs (25).

Consider *SV*-wave propagation through a medium with depth-dependent density $\rho(z)$ and shear-wave velocity $v(z)$ in a flat-earth geometry. The far-field *SV*-wave displacement field in the frequency domain for a shear dislocation point source at $\mathbf{r}_s$ is (Aki & Richards, 1980, eq. 4.88)

$$\mathbf{u}_0(\mathbf{r}, \omega; \mathbf{r}_s, \mathbf{M}) = i\omega \frac{F^{SV}(\hat{\mathbf{M}}, \hat{\mathbf{l}}_0) M(\omega)}{4\pi\rho^{1/2}(z_s)\rho^{1/2}(z)\, v^{5/2}(z_s) v^{1/2}(z)} \frac{1}{\mathrm{R}^S(\mathbf{r}, \mathbf{r}_s)} \exp\left[-i\omega T^S(\mathbf{r}, \mathbf{r}_s)\right] \hat{\mathbf{p}}, \tag{B1}$$

where i denotes the imaginary unit; $\hat{\mathbf{p}}$ is the local perpendicular to the ray (Fig. B1); z_s and z are the source and receiver depths, respectively (Fig. B1); F^{SV} describes the source radiation pattern and depends on the moment tensor geometry $\hat{\mathbf{M}}$ and the initial tangent vector of the ray

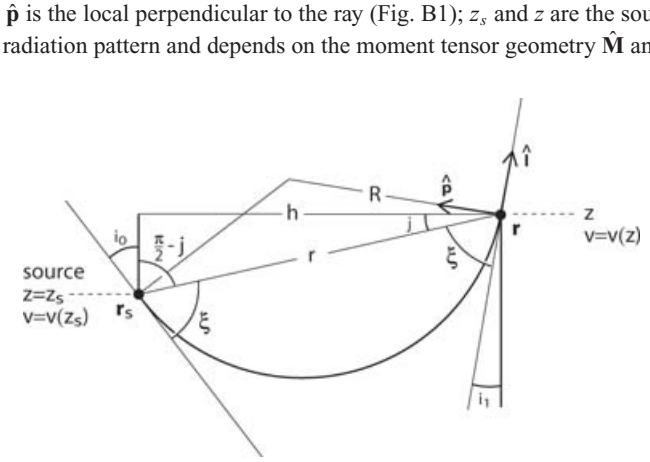

Figure B1. Ray geometry for the case of a constant gradient in depth-dependent wave velocity $v\ (z)$. i_0 and i_1 are incidence angles of the downgoing wave at $\mathbf{r}_s$ and the upgoing wave at $\mathbf{r}$, respectively, and h is the length of the horizontal projection of the line connecting $\mathbf{r}_s$ and $\mathbf{r}$. $\hat{\mathbf{p}}$ and $\hat{\mathbf{l}}$ are the local unit perpendicular and tangent vectors to the ray, with $\hat{\mathbf{p}}$ lying in the vertical plane. The ray path is a circle with constant radius of curvature R.

$\hat{\mathbf{l}}_0$; $M(\omega)$ is the scalar moment spectrum ($\mathbf{M} = M(\omega)\hat{\mathbf{M}}$); $T^S(\mathbf{r}, \mathbf{r}_s)$ is the traveltime from $\mathbf{r}_s$ to $\mathbf{r}$ along the ray; R^S is the geometrical spreading factor.

Let a perturbation $\delta\mathbf{c}$ in the elastic tensor occupy a small volume V centred on a point $\mathbf{r}'$ at depth z'. Under the Born approximation, the scattered wavefield generated by interaction of the incident wavefield with this scatterer may be described as a wavefield propagating on the laterally homogeneous model (i.e. of the form of eq. B1) with moment-tensor source equivalent $\delta\mathbf{M}$ given by (e.g. Hudson 1980)

$$\delta\mathbf{M} = -\delta\mathbf{c}(\mathbf{r}') : \nabla\mathbf{u}_0(\mathbf{r}', \omega; \mathbf{r}_s, \mathbf{M})\, V. \tag{B2}$$

For an isotropic background structure and a shear-velocity perturbation $\delta v\,(\mathbf{r}')$, eqs (B1) and (B2) yield $\delta\mathbf{M}$ with nontrivial component

$$\hat{\mathbf{l}}' \cdot \delta\mathbf{M} \cdot \hat{\mathbf{p}}' = -2\rho(z')\, v(z')\, \delta v(\mathbf{r}') \frac{d}{dl}[\mathbf{u}_0(\mathbf{r}', \omega; \mathbf{r}_s, \mathbf{M}) \cdot \hat{\mathbf{p}}']\, V, \tag{B3}$$

where $\hat{\mathbf{p}}'$ and $\hat{\mathbf{l}}'$ are the local perpendicular and tangent vectors at $\mathbf{r}'$ of the ray connecting $\mathbf{r}_s$ and $\mathbf{r}'$. Integrating over the volume of scatterers, the total wavefield is given by

$$\mathbf{u}(\mathbf{r}, \omega; \mathbf{M}) = \mathbf{u}_0(\mathbf{r}, \omega; \mathbf{M}) + \delta\mathbf{u}(\mathbf{r}, \omega). \tag{B4}$$

$$\delta\mathbf{u}(\mathbf{r}, \omega) = \int \frac{\partial\mathbf{u}_0(\mathbf{r}, \omega; \mathbf{r}', \delta\mathbf{M})}{\partial V}\, d^3\mathbf{r}'. \tag{B5}$$

eqs (B1) and (3) give

$$\frac{d}{dl}(\mathbf{u}_0 \cdot \hat{\mathbf{p}}') = -i\omega \frac{dT^S}{dl}\,(\mathbf{u}_0 \cdot \hat{\mathbf{p}}') = -i\omega \frac{1}{v(z')}(\mathbf{u}_0 \cdot \hat{\mathbf{p}}'). \tag{B6}$$

Substituting eqs (B1) and (B3) into eq. (B5) and making use of eq. (B6) gives

$$\begin{aligned}\delta\mathbf{u}(\mathbf{r}, \omega) = -2\omega^2 \int \rho(z')\, \delta v(\mathbf{r}') &\frac{F^{SV}(\delta\hat{\mathbf{M}}, \hat{\mathbf{l}}')}{4\pi\rho^{1/2}(z')\rho^{1/2}(z)\, v^{5/2}(z')v^{1/2}(z)} \frac{1}{\mathrm{R}^S(\mathbf{r}, \mathbf{r}')} \\ &\times \exp[-i\omega T^S(\mathbf{r}, \mathbf{r}')][\mathbf{u}_0(\mathbf{r}', \omega; \mathbf{r}_s, \mathbf{M}) \cdot \hat{\mathbf{p}}']\hat{\mathbf{p}}''\, d^3\mathbf{r}',\end{aligned} \tag{B7}$$

where $\hat{\mathbf{l}}'$ is the local tangent to the scattered ray path at $\mathbf{r}'$ and $\hat{\mathbf{p}}''$ is the local perpendicular to the scattered ray path at $\mathbf{r}$ along the ray path connecting $\mathbf{r}'$ and $\mathbf{r}$. In the areas around the direct ray where the scattered wave amplitude is above negligible levels, F^{SV} in eq. (B7) may be taken equal to unity (its value on the direct ray path is 1). As a further approximation $\hat{\mathbf{p}}''$ may be equated with the local perpendicular to the direct ray path $\hat{\mathbf{p}}$ at $\mathbf{r}$. The total wavefield is then

$$\begin{aligned}\mathbf{u}(\mathbf{r}, \omega; \mathbf{r}_s, \mathbf{M}) = &\frac{F^{SV}(\hat{\mathbf{M}}, \hat{\mathbf{l}}_0)M(\omega)\, i\omega}{4\pi\rho^{1/2}(z_s)\rho^{1/2}(z)\, v^{5/2}(z_s)v^{1/2}(z)} \frac{1}{\mathrm{R}^S(\mathbf{r}, \mathbf{r}_s)} \exp[-i\omega T^S(\mathbf{r}, \mathbf{r}_s)]\, \hat{\mathbf{p}} \\ &\times \left\{1 - \frac{1}{2\pi}\omega^2 \int \left(\frac{\delta v(\mathbf{r}')}{v(z')}\right) \frac{1}{v^2(z')} \left(\frac{F^{SV}(\hat{\mathbf{M}}, \hat{\mathbf{l}}'_0)}{F^{SV}(\hat{\mathbf{M}}, \hat{\mathbf{l}}_0)}\right) \left(\frac{\mathrm{R}^S(\mathbf{r}, \mathbf{r}_s)}{\mathrm{R}^S(\mathbf{r}', \mathbf{r}_s)\mathrm{R}^S(\mathbf{r}, \mathbf{r}')}\right)\right. \\ &\left. \times \exp[-i\omega\beta(\mathbf{r}, \mathbf{r}_s; \mathbf{r}')]\, d^3\mathbf{r}'\right\},\end{aligned} \tag{B8}$$

where $\hat{\mathbf{l}}'_0$ is the local tangent at the source to the ray path connecting $\mathbf{r}_s$ and $\mathbf{r}'$ and

$$\beta(\mathbf{r}, \mathbf{r}_s; \mathbf{r}') = T^S(\mathbf{r}', \mathbf{r}_s) + T^S(\mathbf{r}, \mathbf{r}') - T^S(\mathbf{r}, \mathbf{r}_s), \tag{B9}$$

is the reduced traveltime of the scattered-wave arrival. (It is also called the "detour time" by Baig *et al.* (2003).) The quantity

$$\frac{F^{SV}(\hat{\mathbf{M}}, \hat{\mathbf{l}}'_0)}{F^{SV}(\hat{\mathbf{M}}, \hat{\mathbf{l}}_0)},$$

accounts for the difference in radiation pattern between the initial ray departing towards $\mathbf{r}'$ and the direct ray departing towards $\mathbf{r}$.

To obtain the Fréchet derivatives for traveltime and amplitude we evaluate the convolutions over frequency given by eqs (25) and isolate the direct arrival with the Hanning function (eq. 34)

$$G(\omega) = \exp[-i\omega T^S(\mathbf{r}, \mathbf{r}_s)]A(\omega, \Delta t). \tag{B10}$$

For a perturbation $\delta v\,(\mathbf{r}')$ over a small volume V, the convolutions are

$$C_{\oplus}(\mathbf{r}, \omega) = \frac{F^{SV}(\hat{\mathbf{M}}, \hat{\mathbf{l}}_0)M(\omega)\, i\omega}{4\pi\rho^{1/2}(z_s)\rho^{1/2}(z)\, v^{5/2}(z_s)v^{1/2}(z)} \frac{1}{\mathrm{R}^S(\mathbf{r}, \mathbf{r}_s)} \exp[-i\omega T^S(\mathbf{r}, \mathbf{r}_s)], \tag{B11}$$

$$\begin{aligned}C_{\oplus+\delta\oplus}(\mathbf{r}, \omega) = &\frac{F^{SV}(\hat{\mathbf{M}}, \hat{\mathbf{l}}_0)M(\omega)\, i\omega}{4\pi\rho^{1/2}(z_s)\rho^{1/2}(z)\, v^{5/2}(z_s)v^{1/2}(z)} \frac{1}{\mathrm{R}^S(\mathbf{r}, \mathbf{r}_s)} \exp[-i\omega T^S(\mathbf{r}, \mathbf{r}_s)] \\ &\times \left\{1 - \frac{1}{2\pi}\omega^2\, a[\beta(\mathbf{r}, \mathbf{r}_s; \mathbf{r}'), \Delta t] \left(\frac{\delta v(\mathbf{r}')}{v(z')}\right) \frac{1}{v^2(z')} \left(\frac{F^{SV}(\hat{\mathbf{M}}, \hat{\mathbf{l}}'_0)}{F^{SV}(\hat{\mathbf{M}}, \hat{\mathbf{l}}_0)}\right)\right. \\ &\left. \times \left(\frac{\mathrm{R}^S(\mathbf{r}, \mathbf{r}_s)}{\mathrm{R}^S(\mathbf{r}', \mathbf{r}_s)\mathrm{R}^S(\mathbf{r}, \mathbf{r}')}\right) \exp[-i\omega\beta(\mathbf{r}, \mathbf{r}_s; \mathbf{r}')]V\right\},\end{aligned} \tag{B12}$$

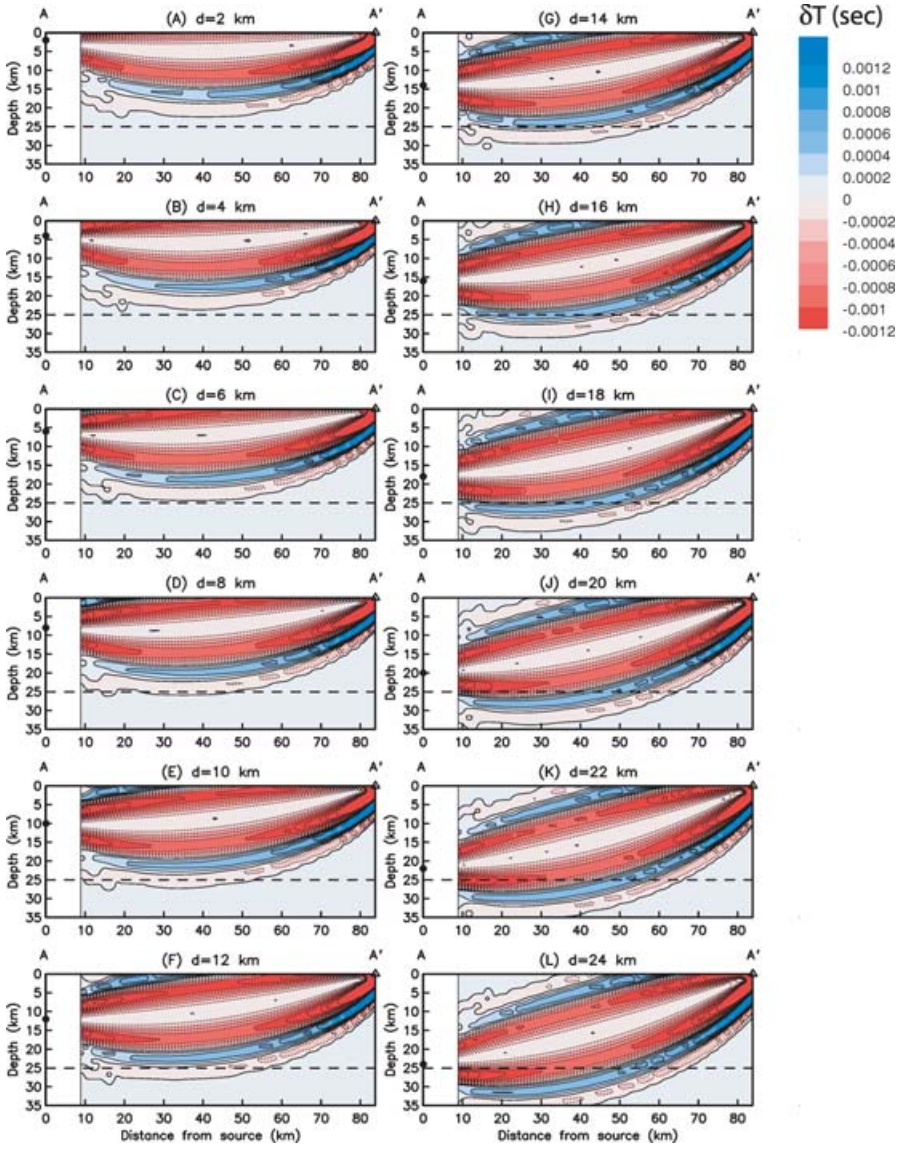

Figure B2. Sensitivity kernels for *S*-wave traveltime on a vertical plane containing the source and receiver (AA' shown in Fig. 5) with indicated source depth d and source–receiver distance 83.9 km. δT is generated using geometrical ray theory. $\delta T = K_{\delta v}^{(\delta T)}\,\delta v V$ is calculated at $\omega = 2\pi$ rad s^{-1}. The source radiation pattern is generated with a non-trivial moment tensor component $M_{r\theta}$, where r measures vertical distance and θ measures distance from the source. In each plot the source is indicated by a filled circle and the receiver by a triangle.

where the Hanning function $a\,(t, \Delta t)$ in the time domain is given by eq. (A2). The resulting amplitude and traveltime sensitivity kernels are

$$K_{\delta v}^{(\delta(\ln A))}(\omega; \mathbf{r}, \mathbf{r}') = -\frac{1}{2\pi}\omega^2\,\frac{1}{v^3(z')}\left(\frac{F^{SV}(\hat{\mathbf{M}}, \hat{\mathbf{l}}_0')}{F^{SV}(\hat{\mathbf{M}}, \hat{\mathbf{l}}_0)}\right)$$
$$\times\left(\frac{\mathrm{R}^S(\mathbf{r}, \mathbf{r}_s)}{\mathrm{R}^S(\mathbf{r}', \mathbf{r}_s)\mathrm{R}^S(\mathbf{r}, \mathbf{r}')}\right)a[\beta(\mathbf{r}, \mathbf{r}_s; \mathbf{r}'), \Delta t]\cos[\omega\beta(\mathbf{r}, \mathbf{r}_s; \mathbf{r}')], \tag{B13}$$

$$K_{\delta v}^{(\delta T)}(\omega; \mathbf{r}, \mathbf{r}') = -\frac{1}{2\pi}\omega\,\frac{1}{v^3(z')}\left(\frac{F^{SV}(\hat{\mathbf{M}}, \hat{\mathbf{l}}_0')}{F^{SV}(\hat{\mathbf{M}}, \hat{\mathbf{l}}_0)}\right)$$
$$\times\left(\frac{\mathrm{R}^S(\mathbf{r}, \mathbf{r}_s)}{\mathrm{R}^S(\mathbf{r}', \mathbf{r}_s)\mathrm{R}^S(\mathbf{r}, \mathbf{r}')}\right)a[\beta(\mathbf{r}, \mathbf{r}_s; \mathbf{r}'), \Delta t]\sin[\omega\beta(\mathbf{r}, \mathbf{r}_s; \mathbf{r}')], \tag{B14}$$

These analytic expressions for $K_{\delta v}^{(\delta(\ln A))}$ and $K_{\delta v}^{(\delta T)}$ exhibit many of the well-known properties of sensitivity kernels. For example, for a scatterer $\mathbf{r}'$ located on the direct ray path connecting $\mathbf{r}_s$ and $\mathbf{r}$, $\beta\,(\mathbf{r}, \mathbf{r}_s; \mathbf{r}') = 0$, and the associated traveltime perturbation is zero and the amplitude perturbation is negative for positive velocity perturbation (i.e. defocussing).

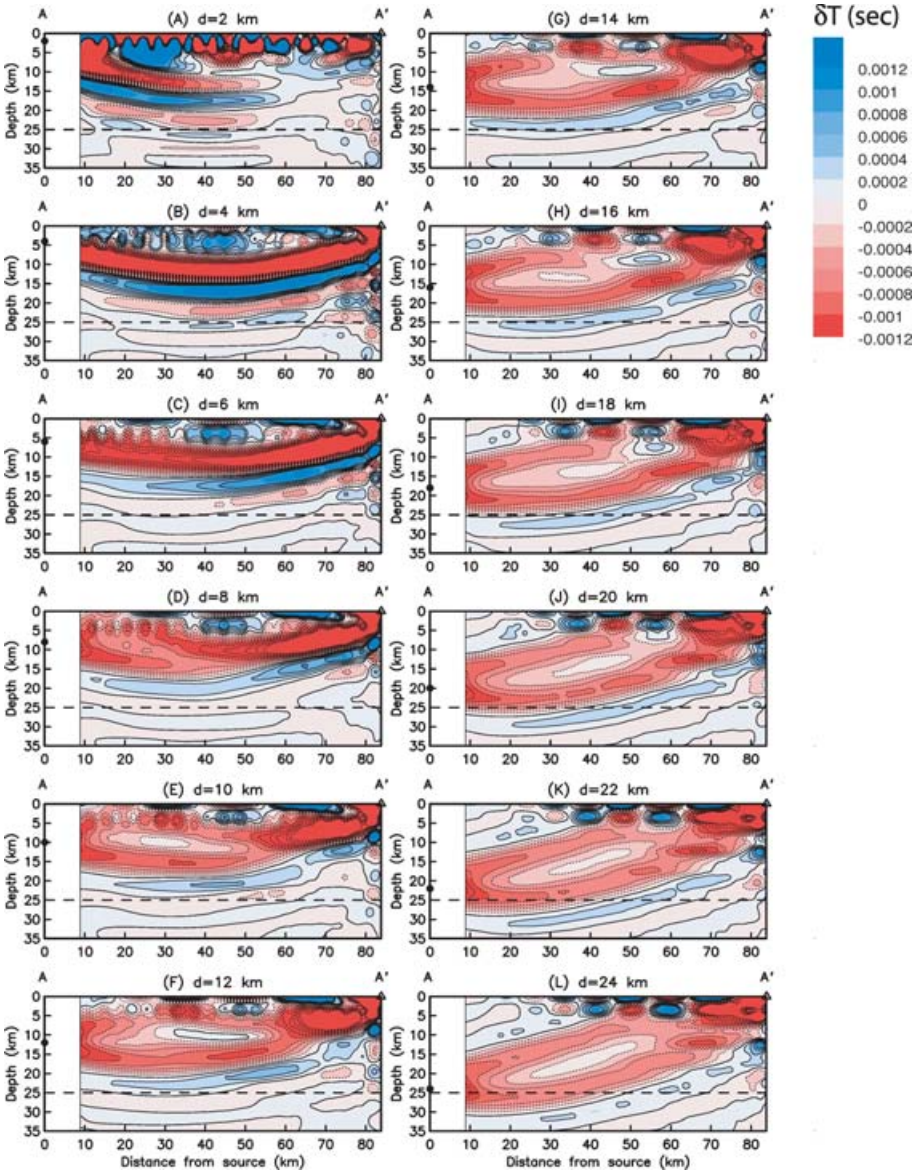

Figure B3. Sensitivity kernel for *S*-wave traveltime on a vertical plane containing the source and receiver (AA′ shown in Fig. 5) with indicated source depth d and source–receiver distance 83.9 km. δT is generated using coupling travelling waves among dispersion branches with horizontal phase velocity less than 5.6 km s^{-1}. $\delta T = K_{\delta v}^{(\delta T)}\,\delta v V$ and $\delta(\ln A) = K_{\delta v}^{(\delta(\ln A))}\,\delta v V$ are calculated at $\omega = 2\pi$ rad s^{-1}. The source radiation pattern is generated with a non-trivial moment tensor component $M_{r\theta}$, where r measures vertical distance and θ measures distance from the source. In each plot the source is indicated by a filled circle and the receiver by a triangle.

B2 High-frequency limit

As $\omega \to \infty$ and $\Delta t \to 0$, the zone of non-negligible contributions to traveltime shift becomes increasingly concentrated near the direct ray path. Let $\mathbf{r}'$ be a point lying on the direct ray path. The sum of the contributions in the vicinity of $\mathbf{r}'$ may be evaluated by integrating $K_{\delta v}^{(\delta T)} \times \delta v$ over a plane containing $\mathbf{r}'$. We parametrize this plane as the set of points $\{\mathbf{r}' + \mathbf{q}\}$ and let ds be the infinitesimal thickness of the volume bounded by two such planes. The contribution to traveltime shift is

$$\delta T = \left\{K_{\delta v}^{(\delta T)}(\omega; \mathbf{r}, \mathbf{r}' + \mathbf{q})\,\delta v(\mathbf{r}' + \mathbf{q})\,d\mathcal{A}\right\} ds, \tag{B15}$$

where $d\mathcal{A} = d^2\mathbf{q}$ is the area element. It is convenient to interpret $d\mathcal{A}$ as the differential area between two ellipses that define reduced traveltimes of β and $\beta + d\beta$. The integral of eq. (B15) is then

$$\delta T = \left\{ \int_0^{\Delta t} K_{\delta v}^{(\delta T)}(\omega; \mathbf{r}, \mathbf{r}' + \mathbf{q})\,\delta v(\mathbf{r}' + \mathbf{q})\,\frac{d\mathcal{A}}{d\beta}\,d\beta \right\} ds. \tag{B16}$$

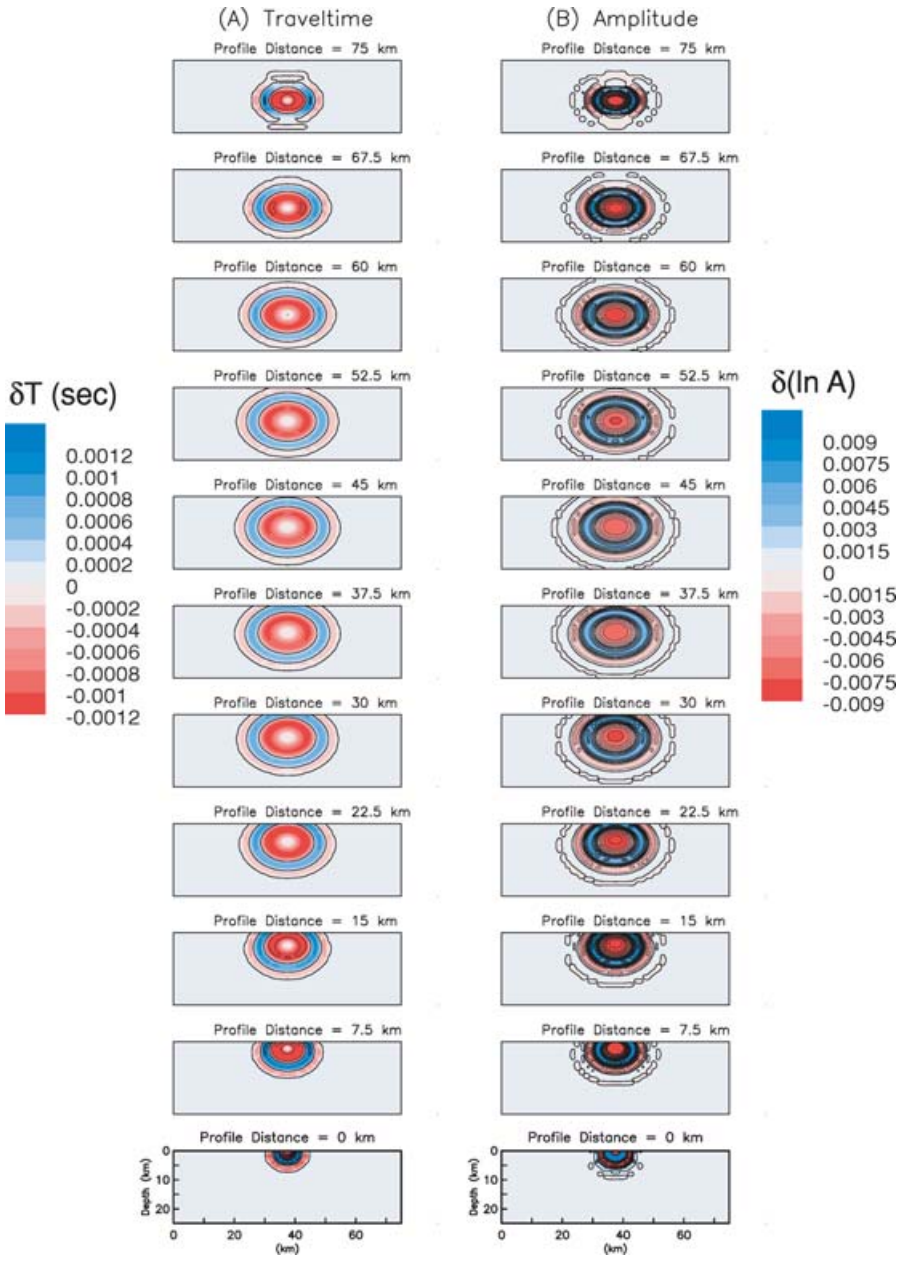

Figure B4. Sensitivity kernels for traveltime (a) and amplitude (b) for the S wave with source depth $d = 20$ km, source–receiver distance 83.9 km, calculated using geometrical ray theory. $\delta T = K_{\delta v}^{(\delta T)}\,\delta v V$ and $\delta(\ln A) = K_{\delta v}^{(\delta(\ln A))}\,\delta v V$ are calculated at $\omega = 2\pi$ rad s^{-1}. The source radiation pattern is generated with a non-trivial moment tensor component $M_{r\theta}$, where r measures vertical distance and θ measures distance from the source. The given profile distance is the distance y of the vertical profile from the receiver (Fig. 5).

The limits of integration correspond to non-vanishing values of a $(\beta,\ \Delta t)$. We may approximate slowly varying quantities $(v, \delta v(\mathbf{r}' + \mathbf{q})/v, F^{SV}(\hat{\mathbf{M}}, \hat{\mathbf{l}}_0'))$ with their values on the direct ray path. Using the relation (eq. 26 of Zhao *et al.* 2000)

$$\frac{d\mathcal{A}}{d\beta} = 2\pi v(z')\left(\frac{\mathrm{R}^S(\mathbf{r}' + \mathbf{q}, \mathbf{r}_s)\mathrm{R}^S(\mathbf{r}, \mathbf{r}' + \mathbf{q})}{\mathrm{R}^S(\mathbf{r}, \mathbf{r}_s)}\right), \tag{B17}$$

and eq. (B14), eq. (B16) becomes

$$\delta T = -\omega\left(\frac{\delta v(\mathbf{r}')}{v(z')}\right)\frac{1}{v(z')}\left\{\int_0^{\Delta t} a[\beta, \Delta t]\sin[\omega\beta]\,d\beta\right\}ds$$

$$= -\omega\left(\frac{\delta v(\mathbf{r}')}{v(z')}\right)\frac{1}{v(z')}\left\{\frac{1}{2\omega}[1 - \cos(\omega\Delta t)] + \frac{1}{4}[1 + \cos(\omega\Delta t)]\right.$$

$$\left.\times\left[\frac{1}{\omega + \omega_{\mathrm{Nyq}}} + \frac{1}{\omega - \omega_{\mathrm{Nyq}}}\right]\right\}ds, \tag{B18}$$

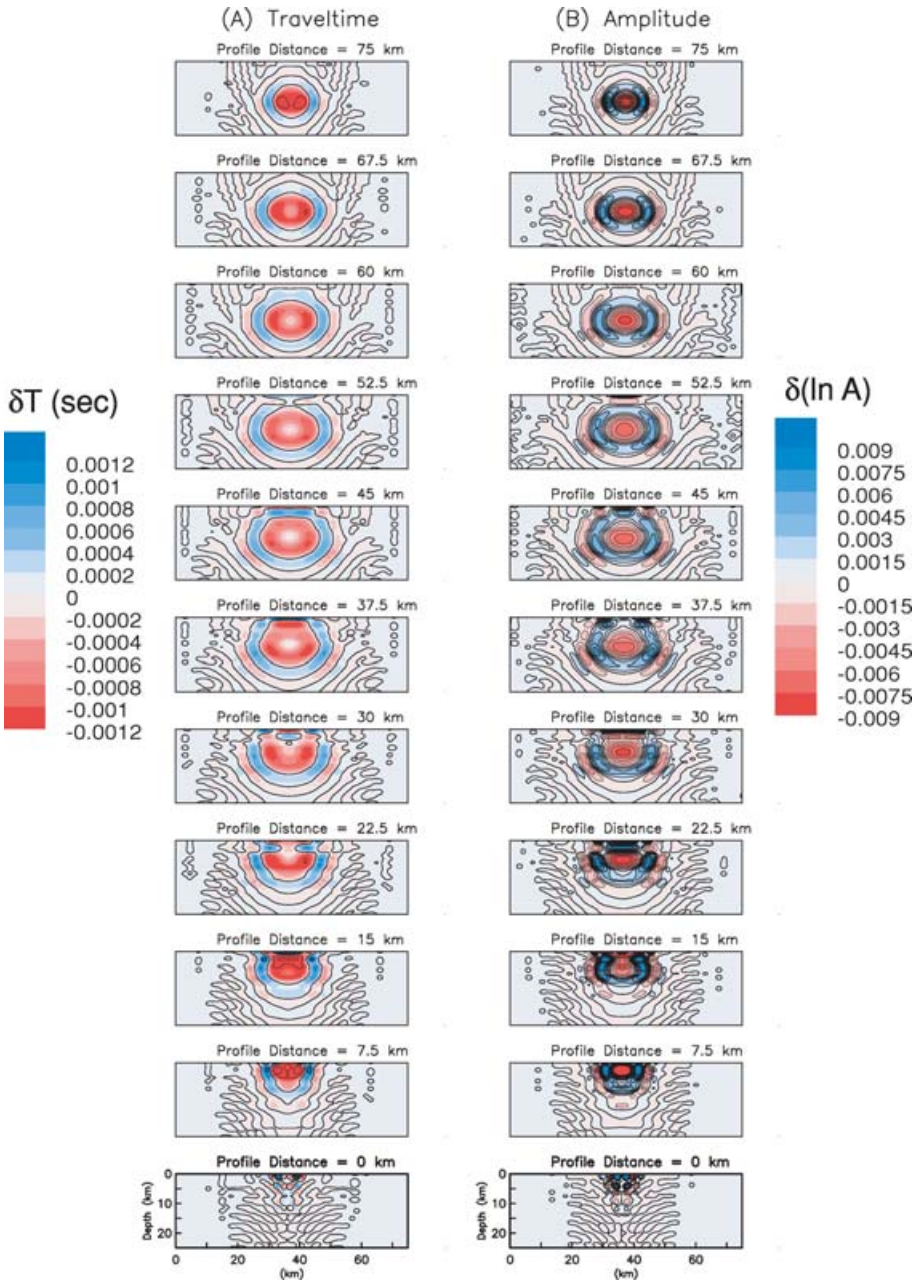

Figure B5. Sensitivity kernels for traveltime (a) and amplitude (b) for the S wave with source depth $d = 20$ km, source–receiver distance 83.9 km, calculated using coupled travelling waves among dispersion branches with horizontal phase velocity less than 5.6 km s^{-1}. $\delta T = K_{\delta v}^{(\delta T)}\,\delta v V$ and $\delta(\ln A) = K_{\delta v}^{(\delta(\ln A))}\,\delta v V$ are calculated at $\omega = 2\pi$ rad s^{-1}. The source radiation pattern is generated with a non-trivial moment tensor component $M_{r\theta}$, where r measures vertical distance and θ measures distance from the source. The given profile distance is the distance y of the vertical profile from the receiver (Fig. 5).

where $\omega_{\rm Nyq} = \pi/\Delta t$ is the Nyquist frequency of the target window. For frequency $\omega \gg \omega_{\rm Nyq}$, eq. (B18) reduces to

$$\delta T = -\left(\frac{\delta v(\mathbf{r}')}{v(z')}\right)\frac{1}{v(z')}\,ds, \tag{B19}$$

which is precisely the contribution from the ray path given by classical ray theory (eq. 2).

B3 Model of constant velocity gradient

We focus on the case of a constant velocity gradient, that is,

$$v(z) = v(z_s) + v'(z - z_s), \tag{B20}$$

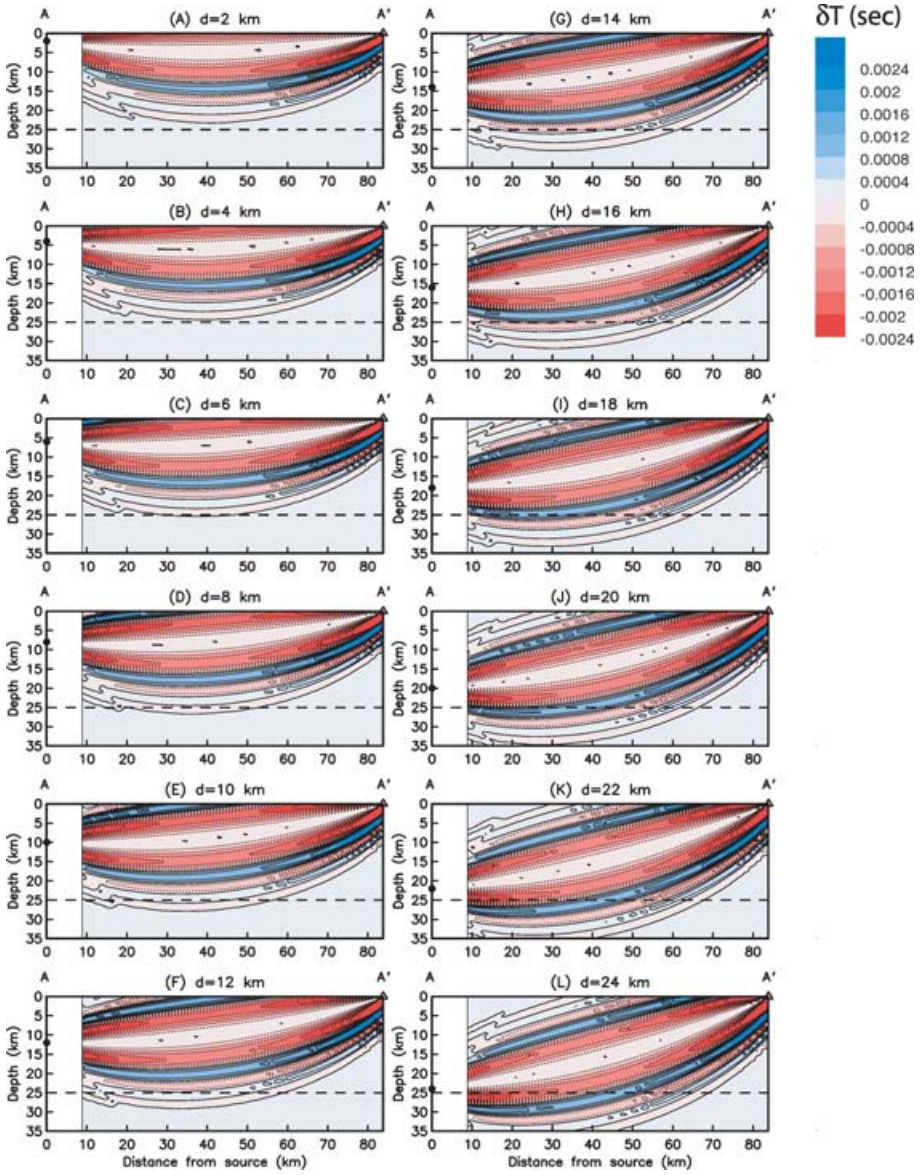

Figure B6. Same as Fig. B2, but $\delta T = K_{\delta v}^{(\delta T)} \delta v V$ is calculated at $\omega = 3\pi$ rad s^{-1}.

where v' is a constant. This case has been previously considered by Hung *et al.* (2000), and in the following we recapitulate several results given in their Appendix A1. It follows from eq. (B20) and Snell's law that the ray paths are circles with constant radius of curvature R given by

$$\frac{1}{R} = pv', \tag{B21}$$

where p is the ray parameter. The requirement that the ray path be circular with radius of curvature given by eq. (B21) allows one to derive the initial incidence angle of the ray. We use the convention that i_0 is the initial incidence angle of the downgoing ray at $\mathbf{r}_s$, and i_1 is the incidence angle of the upgoing ray at $\mathbf{r}$ (Fig. B1). Referring to the quantities in Fig. B1 we may write trigonometric relations

$$\begin{aligned} i_1 &= i_0 - 2j \\ j &= \tan^{-1}\left[\frac{z_s - z}{h}\right] \\ r = |\mathbf{r}_s - \mathbf{r}| &= \sqrt{(z_s - z)^2 + h^2} \\ \xi &= \frac{\pi}{2} - (i_0 - j) \\ \frac{1}{R} &= \frac{2}{r}\sin\xi = \frac{2}{r}\cos(i_0 - j). \end{aligned} \tag{B22}$$

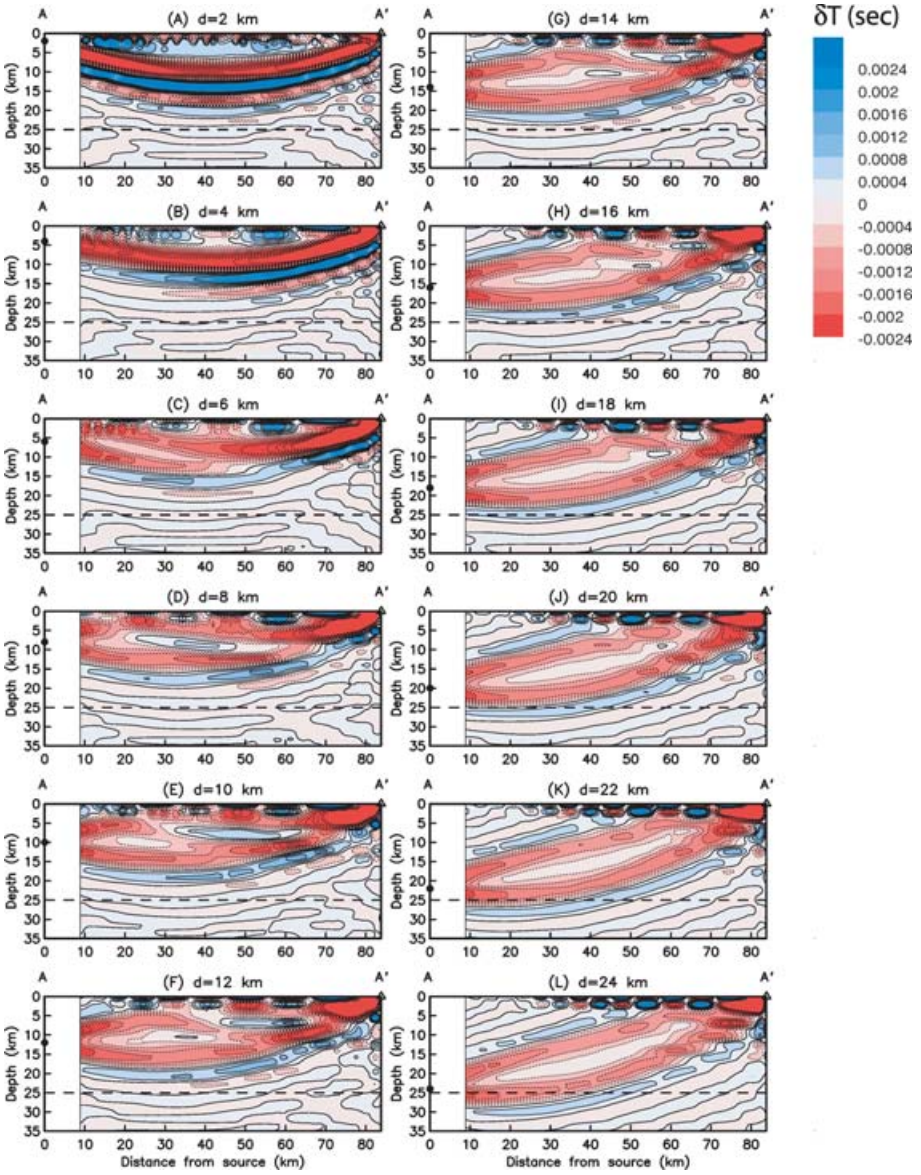

Figure B7. Same as Fig. B3, but $\delta T = K_{\delta v}^{(\delta T)}\, \delta v V$ is calculated at $\omega = 3\pi$ rad s^{-1}.

Using $p = \sin i_0 / v\,(z_s)$ in combination with eqs (B21) and (B22) we find

$$\frac{2}{r}\cos(i_0 - j) = \frac{\sin i_0}{v(z_s)} v', \tag{B23}$$

$$\tan i_0 = \frac{\frac{2}{r}\cos j}{\frac{v'}{v(z_s)} - \frac{2}{r}\sin j} \qquad (0 < i_0 \leq \pi). \tag{B24}$$

The incidence angle obtained in eq. (B24) is used to obtain the radius of curvature via eq. (B21). In the limiting case of $v' = 0$ eq. (B24) would yield $i_0 = \pi/2 + j$, corresponding to a straight line between $\mathbf{r}_s$ and $\mathbf{r}$.

The traveltime is given by

$$T^S = \int_{\text{ray}} \frac{1}{v(z)}\, dl = \int_{\text{ray}} \frac{p}{\sin i}\, dl, \tag{B25}$$

where i is the local incidence angle and dl is a length element along the ray. Let $i = i_0 + \theta$, where θ measures arc length along the circular ray path, and $dl = R\, d\theta$. Then

$$T^S(\mathbf{r}, \mathbf{r}_s) = pR \int_0^{(\pi - i_1) - i_0} \frac{1}{\sin(\theta + i_0)}\, d\theta = pR \ln\left[\frac{\tan(\frac{\pi}{2} - \frac{i_1}{2})}{\tan\left(\frac{i_0}{2}\right)}\right]. \tag{B26}$$

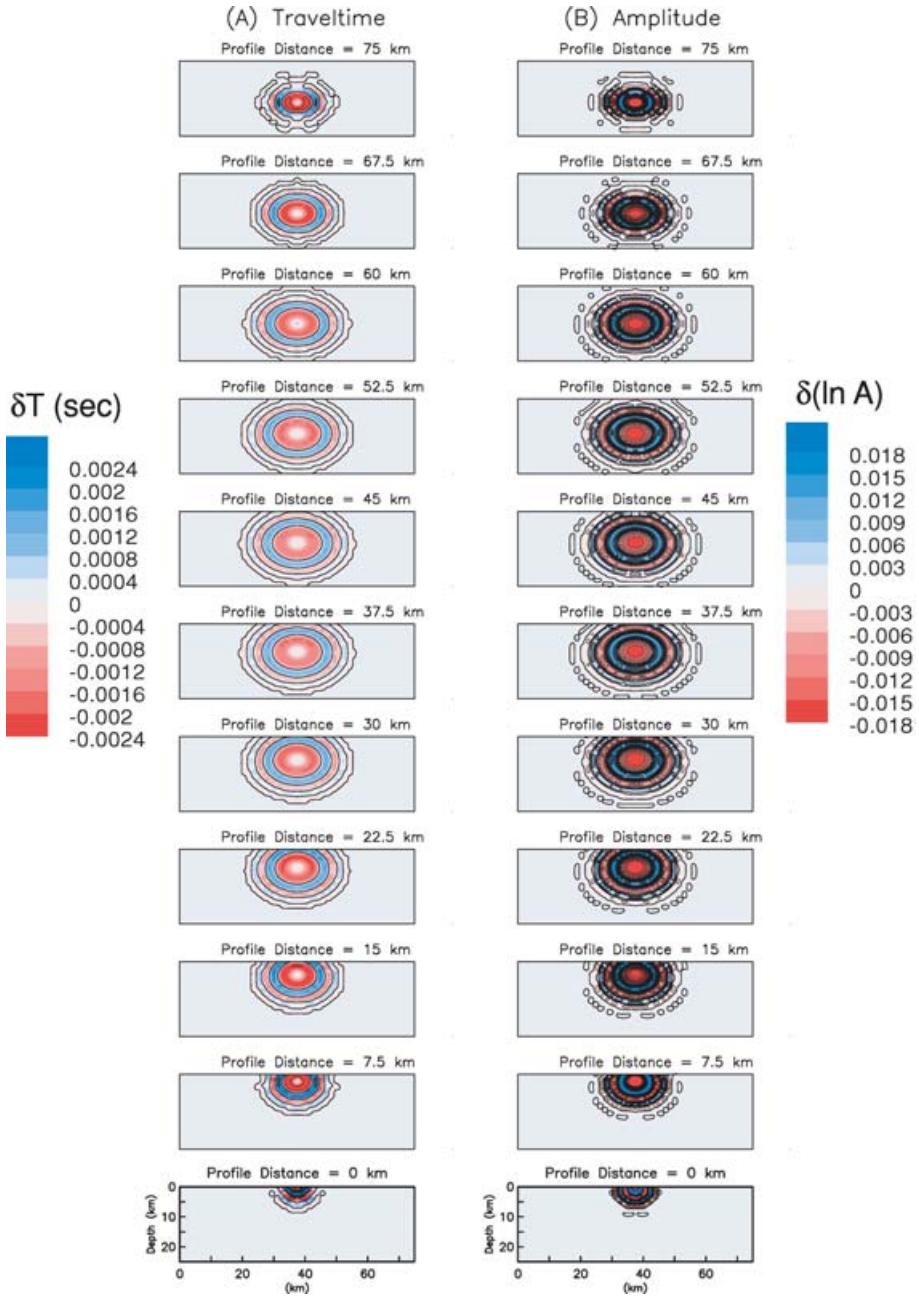

Figure B8. Same as Fig. B4, but $\delta T = K_{\delta v}^{(\delta T)}\,\delta v V$ and $\delta(\ln A) = K_{\delta v}^{(\delta(\ln A))}\,\delta v V$ are calculated at $\omega = 3\pi$ rad s^{-1}.

Substituting for i_1 the first of eqs (B22) into eq. (B26) yields

$$T^S(\mathbf{r}, \mathbf{r}_s) = pR \ln\left[\frac{\tan\left(\frac{\pi}{2} - \frac{i_0}{2} + j\right)}{\tan\left(\frac{i_0}{2}\right)}\right]. \tag{B27}$$

The geometrical spreading factor is given by the ray-tube formula (e.g. eq. 15.97 of Dahlen & Tromp 1998)

$$\mathrm{R}^S(\mathbf{r}, \mathbf{r}_s) = \sqrt{\frac{\Sigma}{\Omega}}, \tag{B28}$$

where Σ is the area at $\mathbf{r}$ of a pencil of rays spreading from $\mathbf{r}_s$ with solid angle Ω. Let δi_0 and $\delta\phi_0$ be the differences in incidence angle and azimuth, respectively, of four rays defining a ray tube, that is, with coordinates at $\mathbf{r}_s$ of (i_0, ϕ_0), $(i_0 + \delta i_0, \phi_0)$, $(i_0, \phi_0 + \delta\phi_0)$, and $(i_0 + \delta i_0, \phi_0 + \delta\phi_0)$. We then have

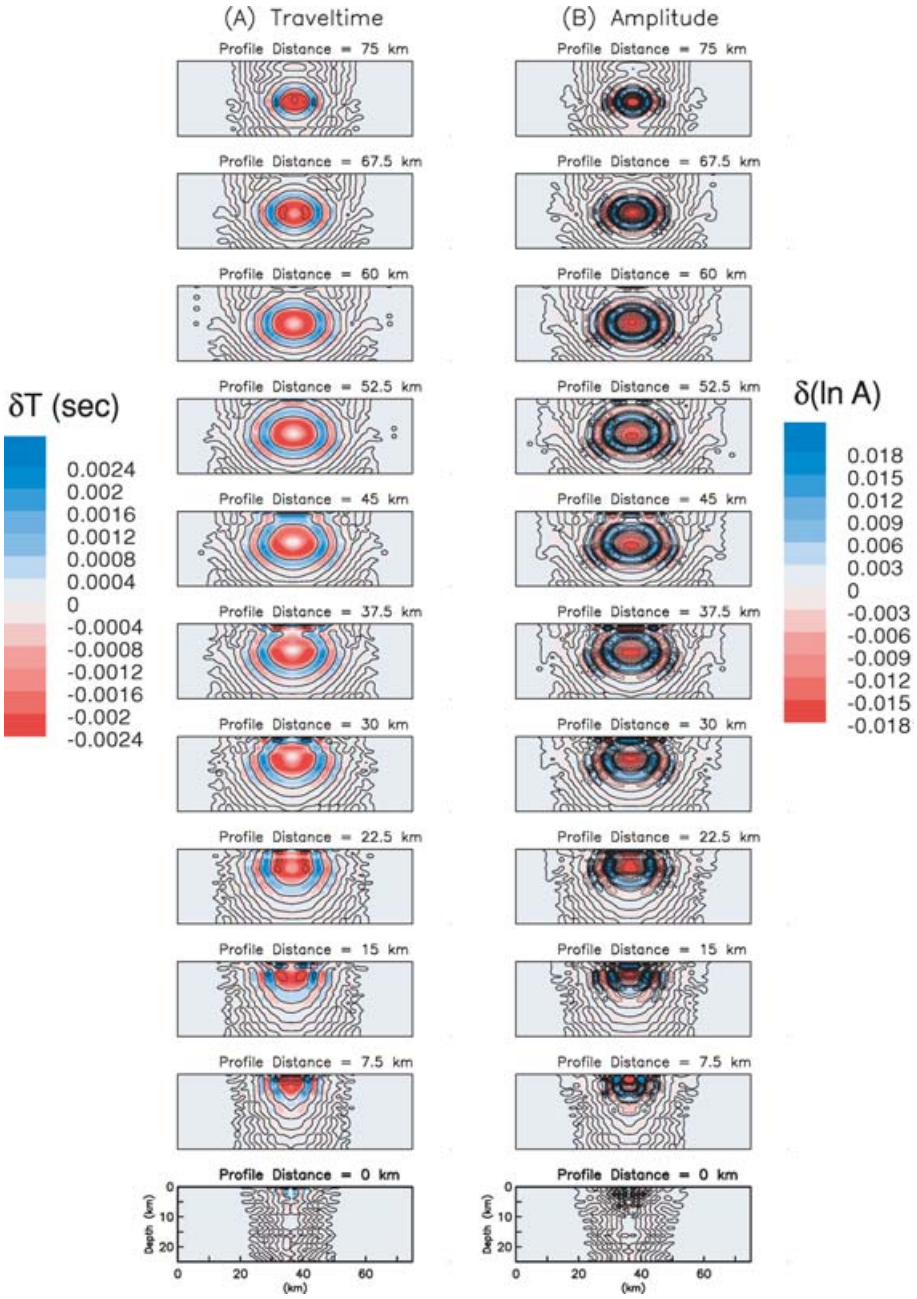

Figure B9. Same as Fig. B5, but $\delta T = K_{\delta v}^{(\delta T)}\,\delta v V$ and $\delta(\ln A) = K_{\delta v}^{(\delta(\ln A))}\,\delta v V$ are calculated at $\omega = 3\pi$ rad s^{-1}.

$$\Sigma = r^2 \csc i_0 \cos^2 j\, \delta i_0\, \delta\phi_0$$
$$\Omega = \sin i_0\, \delta i_0\, \delta\phi_0$$
$$\mathrm{R}^S(\mathbf{r}, \mathbf{r}_s) = r \csc i_0 \cos j. \tag{B29}$$

It is clear that analogous formulae to the above apply to the 'source–receiver' configurations $\mathbf{r}_s$ to $\mathbf{r}'$ and $\mathbf{r}'$ to $\mathbf{r}$, that is, the two ray paths that compose a scattered wave trajectory.

B4 Comparison of travelling wave and ray-theoretical solutions

A synthetic earth model is defined with a gentle S-velocity gradient of 0.0185 km s^{-1} per km depth, increasing from 4.157 km s^{-1} at 0 km depth to 4.619 km/dec at 25 km depth, 5.081 km s^{-1} at 50 km depth, etc.; Poisson's ratio equals 0.25 and density equals a constant 3000 kg-m^{-3}. We prescribe a +12 per cent perturbation in shear-wave velocity over a volume $V = 2.68$ km^3 centred on the target scatterer. Fig. B2 shows examples of $K_{\delta v}^{(\delta T)}\,\delta v V$ at $\omega = 2\pi$ rad s^{-1} for the direct S wave with windows of half-width $\Delta t = 2$ sec centred on the

theoretical arrival time of direct *S* (e.g. eq. B27), generated using geometrical ray theory (eq. B14). The point source corresponds to dip slip on a vertical fault perpendicular to the plane of the profile. Fig. B3 shows the pattern of $K_{\delta v}^{(\delta T)}\,\delta v V$ generated using coupled travelling waves retaining the dispersion branches with horizontal phase velocity less than 5.6 km s^{-1}. Agreement is good for sources deeper than about 12 km. The influence of the free surface becomes increasingly evident for shallower sources. In general the doughnut pattern is disrupted near the receiver and progressively closer to the source region as the source depth is reduced. As in earlier examples (e.g. Sections 5.2 and 5.3), the effects of directly arriving energy from the *sS*, *sP*, and/or surface waves, plus scattered energy from these phases, are the main sources of interference. Figs B4 and B5 show $K_{\delta v}^{(\delta T)}\,\delta v V$ and $K_{\delta v}^{(\delta(\ln A))}\,\delta v V$ along vertical profiles perpendicular to the direct propagation path for the case of source depth $d = 20$ km. It demonstrates good agreement with geometrical ray theory.

Figs B6 and B7 show the corresponding $K_{\delta v}^{(\delta T)}\,\delta v V$ at $\omega = 3\pi$ rad s^{-1} for the various source depths, and Figs B8 and B9 show the associated $K_{\delta v}^{(\delta T)}\,\delta v V$ and $K_{\delta v}^{(\delta(\ln A))}\,\delta v V$ on vertical profiles perpendicular to the direct propagation path. Comparison with Figs B2–B5 reveals that the widths of the alternating bands of positive and negative $K_{\delta v}^{(\delta T)}$ are smaller and the amplitudes of $K_{\delta v}^{(\delta T)}$ and $K_{\delta v}^{(\delta(\ln A))}$ are higher. The different sensitivity patterns at different ω illustrate the potential for using frequency-dependent traveltime kernels to extract more constraints on structural perturbations from a set of seismograms.